The characterization of Virgo data and its impact on gravitational-wave searches.

J. Aasi[1], J. Abadie[1], B. P. Abbott[1], R. Abbott[1], T. D. Abbott[2],
M. Abernathy[3], T. Accadia[4], F. Acernese[5ac], C. Adams[6],
T. Adams[7], P. Addesso[58], R. Adhikari[1], C. Affeldt[9,10],
M. Agathos[11a], K. Agatsuma[12], P. Ajith[1], B. Allen[9,13,10],
A. Allocca[14ac], E. Amador Ceron[13], D. Amariutei[15],
S. B. Anderson[1], W. G. Anderson[13], K. Arai[1], M. C. Araya[1],
S. Ast[9,10], S. M. Aston[6], P. Astone[16a], D. Atkinson[17],
P. Aufmuth[10,9], C. Aulbert[9,10], B. E. Aylott[18], S. Babak[19],
P. Baker[20], G. Ballardin[21], T. Ballinger[55], S. Ballmer[22],
Y. Bao[15], J. C. B. Barayoga[1], D. Barker[17], F. Barone[5ac],
B. Barr[3], L. Barsotti[23], M. Barsuglia[24], M. A. Barton[17],
I. Bartos[25], R. Bassiri[3,26], M. Bastarrika[3], A. Basti[14ab],
J. Batch[17], J. Bauchrowitz[9,10], Th. S. Bauer[11a], M. Bebronne[4],
D. Beck[26], B. Behnke[19], M. Bejger[27c], M.G. Beker[11a],
A. S. Bell[3], C. Bell[3], I. Belopolski[25], M. Benacquista[28],
J. M. Berliner[17], A. Bertolini[9,10], J. Betzwieser[6], N. Beveridge[3],
P. T. Beyersdorf[29], T. Bhadbade[26], I. A. Bilenko[30],
G. Billingsley[1], J. Birch[6], R. Biswas[28], M. Bitossi[14a],
M. A. Bizouard[31a], E. Black[1], J. K. Blackburn[1], L. Blackburn[32],
D. Blair[33], B. Bland[17], M. Blom[11a], O. Bock[9,10], T. P. Bodiya[23],
C. Bogan[9,10], C. Bond[18], R. Bondarescu[34], F. Bondu[35b],
L. Bonelli[14ab], R. Bonnand[36], R. Bork[1], M. Born[9,10],
V. Boschi[14a], S. Bose[37], L. Bosi[38a], B. Bouhou[24], S. Braccini[14a],
C. Bradaschia[14a], P. R. Brady[13], V. B. Braginsky[30],
M. Branchesi[39ab], J. E. Brau[40], J. Breyer[9,10], T. Briant[41],
D. O. Bridges[6], A. Brillet[35a], M. Brinkmann[9,10], V. Brisson[31a],
M. Britzger[9,10], A. F. Brooks[1], D. A. Brown[22], T. Bulik[27b],
H. J. Bulten[11ab], A. Buonanno[42], J. Burguet–Castell[43],
D. Buskulic[4], C. Buy[24], R. L. Byer[26], L. Cadonati[44],
G. Cagnoli[28,36], E. Calloni[5ab], J. B. Camp[32], P. Campsie[3],
K. Cannon[45], B. Canuel[21], J. Cao[46], C. D. Capano[42],
F. Carbognani[21], L. Carbone[18], S. Caride[47], S. Caudill[48],
M. Cavaglià[49], F. Cavalier[31a], R. Cavalieri[21], G. Cella[14a],
C. Cepeda[1], E. Cesarini[39b], T. Chalermsongsak[1], P. Charlton[50],
E. Chassande-Mottin[24], W. Chen[46], X. Chen[33], Y. Chen[51],

A. Chincarini[52], A. Chiummo[21], H. S. Cho[53], J. Chow[54],
N. Christensen[55], S. S. Y. Chua[54], C. T. Y. Chung[56],
S. Chung[33], G. Ciani[15], F. Clara[17], D. E. Clark[26], J. A. Clark[44],
J. H. Clayton[13], F. Cleva[35a], E. Coccia[57ab], P.-F. Cohadon[41],
C. N. Colacino[14ab], A. Colla[16ab], M. Colombini[16b], A. Conte[16ab],
R. Conte[58], D. Cook[17], T. R. Corbitt[23], M. Cordier[29],
N. Cornish[20], A. Corsi[1], C. A. Costa[48,59], M. Coughlin[55],
J.-P. Coulon[35a], P. Couvares[22], D. M. Coward[33], M. Cowart[6],
D. C. Coyne[1], J. D. E. Creighton[13], T. D. Creighton[28],
A. M. Cruise[18], A. Cumming[3], L. Cunningham[3], E. Cuoco[21],
R. M. Cutler[18], K. Dahl[9,10], M. Damjanic[9,10], S. L. Danilishin[33],
S. D'Antonio[57a], K. Danzmann[9,10], V. Dattilo[21], B. Daudert[1],
H. Daveloza[28], M. Davier[31a], E. J. Daw[60], R. Day[21],
T. Dayanga[37], R. De Rosa[5ab], D. DeBra[26], G. Debreczeni[61],
J. Degallaix[36], W. Del Pozzo[11a], T. Dent[7], V. Dergachev[1],
R. DeRosa[48], S. Dhurandhar[62], L. Di Fiore[5a], A. Di Lieto[14ab],
I. Di Palma[9,10], M. Di Paolo Emilio[57ac], A. Di Virgilio[14a],
M. Díaz[28], A. Dietz[4,49], F. Donovan[23], K. L. Dooley[9,10],
S. Doravari[1], S. Dorsher[63], M. Drago[64ab], R. W. P. Drever[65],
J. C. Driggers[1], Z. Du[46], J.-C. Dumas[33], S. Dwyer[23],
T. Eberle[9,10], M. Edgar[3], M. Edwards[7], A. Effler[48], P. Ehrens[1],
G. Endrőczi[61], R. Engel[1], T. Etzel[1], K. Evans[3], M. Evans[23],
T. Evans[6], M. Factourovich[25], V. Fafone[57ab], S. Fairhurst[7],
B. F. Farr[66], M. Favata[13], D. Fazi[66], H. Fehrmann[9,10],
D. Feldbaum[15], I. Ferrante[14ab], F. Ferrini[21], F. Fidecaro[14ab],
L. S. Finn[34], I. Fiori[21], R. P. Fisher[22], R. Flaminio[36], S. Foley[23],
E. Forsi[6], L. A. Forte[5a], N. Fotopoulos[1], J.-D. Fournier[35a],
J. Franc[36], S. Franco[31a], S. Frasca[16ab], F. Frasconi[14a],
M. Frede[9,10], M. A. Frei[67], Z. Frei[68], A. Freise[18], R. Frey[40],
T. T. Fricke[9,10], D. Friedrich[9,10], P. Fritschel[23], V. V. Frolov[6],
M.-K. Fujimoto[12], P. J. Fulda[18], M. Fyffe[6], J. Gair[69],
M. Galimberti[36], L. Gammaitoni[38ab], J. Garcia[17], F. Garufi[5ab],
M. E. Gáspár[61], G. Gelencser[68], G. Gemme[52], E. Genin[21],
A. Gennai[14a], L. Á. Gergely[70], S. Ghosh[37], J. A. Giaime[48,6],
S. Giampanis[13], K. D. Giardina[6], A. Giazotto[14a],
S. Gil-Casanova[43], C. Gill[3], J. Gleason[15], E. Goetz[9,10],
G. González[48], M. L. Gorodetsky[30], S. Goßler[9,10], R. Gouaty[4],
C. Graef[9,10], P. B. Graff[69], M. Granata[36], A. Grant[3], C. Gray[17],
R. J. S. Greenhalgh[71], A. M. Gretarsson[72], C. Griffo[2],
H. Grote[9,10], K. Grover[18], S. Grunewald[19], G. M. Guidi[39ab],
C. Guido[6], R. Gupta[62], E. K. Gustafson[1], R. Gustafson[47],
J. M. Hallam[18], D. Hammer[13], G. Hammond[3], J. Hanks[17],

C. Hanna[1,73], J. Hanson[6], A. Hardt[55], J. Harms[65],
G. M. Harry[74], I. W. Harry[22], E. D. Harstad[40],
M. T. Hartman[15], K. Haughian[3], K. Hayama[12], J.-F. Hayau[35b],
J. Heefner[1], A. Heidmann[41], M. C. Heintze[6], H. Heitmann[35a],
P. Hello[31a], G. Hemming[21], M. A. Hendry[3], I. S. Heng[3],
A. W. Heptonstall[1], V. Herrera[26], M. Heurs[9,10],
M. Hewitson[9,10], S. Hild[3], D. Hoak[44], K. A. Hodge[1], K. Holt[6],
M. Holtrop[75], T. Hong[51], S. Hooper[33], J. Hough[3],
E. J. Howell[33], B. Hughey[13], S. Husa[43], S. H. Huttner[3],
T. Huynh-Dinh[6], D. R. Ingram[17], R. Inta[54], T. Isogai[55],
A. Ivanov[1], K. Izumi[12], M. Jacobson[1], E. James[1], Y. J. Jang[66],
P. Jaranowski[27d], E. Jesse[72], W. W. Johnson[48], D. I. Jones[76],
R. Jones[3], R.J.G. Jonker[11a], L. Ju[33], P. Kalmus[1], V. Kalogera[66],
S. Kandhasamy[63], G. Kang[77], J. B. Kanner[42,32],
M. Kasprzack[21,31a], R. Kasturi[78], E. Katsavounidis[23],
W. Katzman[6], H. Kaufer[9,10], K. Kaufman[51], K. Kawabe[17],
S. Kawamura[12], F. Kawazoe[9,10], D. Keitel[9,10], D. Kelley[22],
W. Kells[1], D. G. Keppel[1], Z. Keresztes[70], A. Khalaidovski[9,10],
F. Y. Khalili[30], E. A. Khazanov[79], B. K. Kim[77], C. Kim[80],
H. Kim[9,10], K. Kim[81], N. Kim[26], Y. M. Kim[53], P. J. King[1],
D. L. Kinzel[6], J. S. Kissel[23], S. Klimenko[15], J. Kline[13],
K. Kokeyama[48], V. Kondrashov[1], S. Koranda[13], W. Z. Korth[1],
I. Kowalska[27b], D. Kozak[1], V. Kringel[9,10], B. Krishnan[19],
A. Królak[27ae], G. Kuehn[9,10], P. Kumar[22], R. Kumar[3],
R. Kurdyumov[26], P. Kwee[23], P. K. Lam[54], M. Landry[17],
A. Langley[65], B. Lantz[26], N. Lastzka[9,10], C. Lawrie[3],
A. Lazzarini[1], A. Le Roux[6], P. Leaci[19], C. H. Lee[53], H. K. Lee[81],
H. M. Lee[82], J. R. Leong[9,10], I. Leonor[40], N. Leroy[31a],
N. Letendre[4], V. Lhuillier[17], J. Li[46], T. G. F. Li[11a],
P. E. Lindquist[1], V. Litvine[1], Y. Liu[46], Z. Liu[15],
N. A. Lockerbie[83], D. Lodhia[18], J. Logue[3], M. Lorenzini[39a],
V. Loriette[31b], M. Lormand[6], G. Losurdo[39a], J. Lough[22],
M. Lubinski[17], H. Lück[9,10], A. P. Lundgren[9,10], J. Macarthur[3],
E. Macdonald[3], B. Machenschalk[9,10], M. MacInnis[23],
D. M. Macleod[7], M. Mageswaran[1], K. Mailand[1],
E. Majorana[16a], I. Maksimovic[31b], V. Malvezzi[57a], N. Man[35a],
I. Mandel[18], V. Mandic[63], M. Mantovani[14a], F. Marchesoni[38ac],
F. Marion[4], S. Márka[25], Z. Márka[25], A. Markosyan[26], E. Maros[1],
J. Marque[21], F. Martelli[39ab], I. W. Martin[3], R. M. Martin[15],
J. N. Marx[1], K. Mason[23], A. Masserot[4], F. Matichard[23],
L. Matone[25], R. A. Matzner[84], N. Mavalvala[23], G. Mazzolo[9,10],
R. McCarthy[17], D. E. McClelland[54], S. C. McGuire[85],

G. McIntyre[1], J. McIver[44], G. D. Meadors[47], M. Mehmet[9,10],
T. Meier[10,9], A. Melatos[56], A. C. Melissinos[86], G. Mendell[17],
D. F. Menéndez[34], R. A. Mercer[13], S. Meshkov[1], C. Messenger[7],
M. S. Meyer[6], H. Miao[51], C. Michel[36], L. Milano[5ab], J. Miller[54],
Y. Minenkov[57a], C. M. F. Mingarelli[18], V. P. Mitrofanov[30],
G. Mitselmakher[15], R. Mittleman[23], B. Moe[13], M. Mohan[21],
S. R. P. Mohapatra[44], D. Moraru[17], G. Moreno[17],
N. Morgado[36], A. Morgia[57ab], T. Mori[12], S. R. Morriss[28],
S. Mosca[5ab], K. Mossavi[9,10], B. Mours[4], C. M. Mow–Lowry[54],
C. L. Mueller[15], G. Mueller[15], S. Mukherjee[28], A. Mullavey[48,54],
H. Müller-Ebhardt[9,10], J. Munch[87], D. Murphy[25],
P. G. Murray[3], A. Mytidis[15], T. Nash[1], L. Naticchioni[16ab],
V. Necula[15], J. Nelson[3], I. Neri[38ab], G. Newton[3], T. Nguyen[54],
A. Nishizawa[12], A. Nitz[22], F. Nocera[21], D. Nolting[6],
M. E. Normandin[28], L. Nuttall[7], E. Ochsner[13], J. O'Dell[71],
E. Oelker[23], G. H. Ogin[1], J. J. Oh[88], S. H. Oh[88],
R. G. Oldenberg[13], B. O'Reilly[6], R. O'Shaughnessy[13],
C. Osthelder[1], C. D. Ott[51], D. J. Ottaway[87], R. S. Ottens[15],
H. Overmier[6], B. J. Owen[34], A. Page[18], L. Palladino[57ac],
C. Palomba[16a], Y. Pan[42], C. Pankow[13], F. Paoletti[14a,21],
R. Paoletti[14ac], M. A. Papa[19,13], M. Parisi[5ab], A. Pasqualetti[21],
R. Passaquieti[14ab], D. Passuello[14a], M. Pedraza[1], S. Penn[78],
A. Perreca[22], G. Persichetti[5ab], M. Phelps[1], M. Pichot[35a],
M. Pickenpack[9,10], F. Piergiovanni[39ab], V. Pierro[8], M. Pihlaja[63],
L. Pinard[36], I. M. Pinto[8], M. Pitkin[3], H. J. Pletsch[9,10],
M. V. Plissi[3], R. Poggiani[14ab], J. Pöld[9,10], F. Postiglione[58],
C. Poux[1], M. Prato[52], V. Predoi[7], T. Prestegard[63], L. R. Price[1],
M. Prijatelj[9,10], M. Principe[8], S. Privitera[1], R. Prix[9,10],
G. A. Prodi[64ab], L. G. Prokhorov[30], O. Puncken[9,10],
M. Punturo[38a], P. Puppo[16a], V. Quetschke[28],
R. Quitzow-James[40], F. J. Raab[17], D. S. Rabeling[11ab], I. Rácz[61],
H. Radkins[17], P. Raffai[25,68], M. Rakhmanov[28], C. Ramet[6],
B. Rankins[49], P. Rapagnani[16ab], V. Raymond[66], V. Re[57ab],
C. M. Reed[17], T. Reed[89], T. Regimbau[35a], S. Reid[3],
D. H. Reitze[1], F. Ricci[16ab], R. Riesen[6], K. Riles[47], M. Roberts[26],
N. A. Robertson[1,3], F. Robinet[31a], C. Robinson[7],
E. L. Robinson[19], A. Rocchi[57a], S. Roddy[6], C. Rodriguez[66],
M. Rodruck[17], L. Rolland[4], J. G. Rollins[1], J. D. Romano[28],
R. Romano[5ac], J. H. Romie[6], D. Rosińska[27cf], C. Röver[9,10],
S. Rowan[3], A. Rüdiger[9,10], P. Ruggi[21], K. Ryan[17], F. Salemi[9,10],
L. Sammut[56], V. Sandberg[17], S. Sankar[23], V. Sannibale[1],
L. Santamaría[1], I. Santiago-Prieto[3], G. Santostasi[90],

E. Saracco[36], B. Sassolas[36], B. S. Sathyaprakash[7],
P. R. Saulson[22], R. L. Savage[17], R. Schilling[9,10], R. Schnabel[9,10],
R. M. S. Schofield[40], B. Schulz[9,10], B. F. Schutz[19,7],
P. Schwinberg[17], J. Scott[3], S. M. Scott[54], F. Seifert[1],
D. Sellers[6], D. Sentenac[21], A. Sergeev[79], D. A. Shaddock[54],
M. Shaltev[9,10], B. Shapiro[23], P. Shawhan[42], D. H. Shoemaker[23],
T. L Sidery[18], X. Siemens[13], D. Sigg[17], D. Simakov[9,10],
A. Singer[1], L. Singer[1], A. M. Sintes[43], G. R. Skelton[13],
B. J. J. Slagmolen[54], J. Slutsky[48], J. R. Smith[2], M. R. Smith[1],
R. J. E. Smith[18], N. D. Smith-Lefebvre[23], K. Somiya[51],
B. Sorazu[3], F. C. Speirits[3], L. Sperandio[57ab], M. Stefszky[54],
E. Steinert[17], J. Steinlechner[9,10], S. Steinlechner[9,10],
S. Steplewski[37], A. Stochino[1], R. Stone[28], K. A. Strain[3],
S. E. Strigin[30], A. S. Stroeer[28], R. Sturani[39ab], A. L. Stuver[6],
T. Z. Summerscales[91], M. Sung[48], S. Susmithan[33], P. J. Sutton[7],
B. Swinkels[21], G. Szeifert[68], M. Tacca[21], L. Taffarello[64c],
D. Talukder[37], D. B. Tanner[15], S. P. Tarabrin[9,10], R. Taylor[1],
A. P. M. ter Braack[11a], P. Thomas[17], K. A. Thorne[6],
K. S. Thorne[51], E. Thrane[63], A. Thüring[10,9], C. Titsler[34],
K. V. Tokmakov[83], C. Tomlinson[60], A. Toncelli[14ab],
M. Tonelli[14ab], O. Torre[14ac], C. V. Torres[28], C. I. Torrie[1,3],
E. Tournefier[4], F. Travasso[38ab], G. Traylor[6], M. Tse[25],
E. Tucker[55], D. Ugolini[92], H. Vahlbruch[10,9], G. Vajente[14ab],
J. F. J. van den Brand[11ab], C. Van Den Broeck[11a],
S. van der Putten[11a], A. A. van Veggel[3], S. Vass[1], M. Vasuth[61],
R. Vaulin[23], M. Vavoulidis[31a], A. Vecchio[18], G. Vedovato[64c],
J. Veitch[7], P. J. Veitch[87], K. Venkateswara[93], D. Verkindt[4],
F. Vetrano[39ab], A. Viceré[39ab], A. E. Villar[1], J.-Y. Vinet[35a],
S. Vitale[11a], H. Vocca[38a], C. Vorvick[17], S. P. Vyatchanin[30],
A. Wade[54], L. Wade[13], M. Wade[13], S. J. Waldman[23],
L. Wallace[1], Y. Wan[46], M. Wang[18], X. Wang[46], A. Wanner[9,10],
R. L. Ward[24], M. Was[31a], M. Weinert[9,10], A. J. Weinstein[1],
R. Weiss[23], T. Welborn[6], L. Wen[51,33], P. Wessels[9,10], M. West[22],
T. Westphal[9,10], K. Wette[9,10], J. T. Whelan[67],
S. E. Whitcomb[1,33], D. J. White[60], B. F. Whiting[15],
K. Wiesner[9,10], C. Wilkinson[17], P. A. Willems[1], L. Williams[15],
R. Williams[1], B. Willke[9,10], M. Wimmer[9,10], L. Winkelmann[9,10],
W. Winkler[9,10], C. C. Wipf[23], A. G. Wiseman[13], H. Wittel[9,10],
G. Woan[3], R. Wooley[6], J. Worden[17], J. Yablon[66], I. Yakushin[6],
H. Yamamoto[1], K. Yamamoto[64bd], C. C. Yancey[42], H. Yang[51],
D. Yeaton-Massey[1], S. Yoshida[94], M. Yvert[4], A. Zadrożny[27e],
M. Zanolin[72], J.-P. Zendri[64c], F. Zhang[46], L. Zhang[1], C. Zhao[33],

N. Zotov[89], M. E. Zucker[23], J. Zweizig[1]

[1]LIGO - California Institute of Technology, Pasadena, CA 91125, USA
[2]California State University Fullerton, Fullerton CA 92831 USA
[3]SUPA, University of Glasgow, Glasgow, G12 8QQ, United Kingdom
[4]Laboratoire d'Annecy-le-Vieux de Physique des Particules (LAPP), Université de Savoie, CNRS/IN2P3, F-74941 Annecy-Le-Vieux, France
[5]INFN, Sezione di Napoli [a]; Università di Napoli 'Federico II'[b], Complesso Universitario di Monte S.Angelo, I-80126 Napoli; Università di Salerno, Fisciano, I-84084 Salerno[c], Italy
[6]LIGO - Livingston Observatory, Livingston, LA 70754, USA
[7]Cardiff University, Cardiff, CF24 3AA, United Kingdom
[8]University of Sannio at Benevento, I-82100 Benevento, Italy and INFN (Sezione di Napoli), Italy
[9]Albert-Einstein-Institut, Max-Planck-Institut für Gravitationsphysik, D-30167 Hannover, Germany
[10]Leibniz Universität Hannover, D-30167 Hannover, Germany
[11]Nikhef, Science Park, Amsterdam, the Netherlands[a]; VU University Amsterdam, De Boelelaan 1081, 1081 HV Amsterdam, the Netherlands[b]
[12]National Astronomical Observatory of Japan, Tokyo 181-8588, Japan
[13]University of Wisconsin–Milwaukee, Milwaukee, WI 53201, USA
[14]INFN, Sezione di Pisa[a]; Università di Pisa[b]; I-56127 Pisa; Università di Siena, I-53100 Siena[c], Italy
[15]University of Florida, Gainesville, FL 32611, USA
[16]INFN, Sezione di Roma[a]; Università 'La Sapienza'[b], I-00185 Roma, Italy
[17]LIGO - Hanford Observatory, Richland, WA 99352, USA
[18]University of Birmingham, Birmingham, B15 2TT, United Kingdom
[19]Albert-Einstein-Institut, Max-Planck-Institut für Gravitationsphysik, D-14476 Golm, Germany
[20]Montana State University, Bozeman, MT 59717, USA
[21]European Gravitational Observatory (EGO), I-56021 Cascina (PI), Italy
[22]Syracuse University, Syracuse, NY 13244, USA
[23]LIGO - Massachusetts Institute of Technology, Cambridge, MA 02139, USA
[24]APC, AstroParticule et Cosmologie, Université Paris Diderot, CNRS/IN2P3, CEA/Irfu, Observatoire de Paris, Sorbonne Paris Cité, 10, rue Alice Domon et Léonie Duquet, 75205 Paris Cedex 13, France
[25]Columbia University, New York, NY 10027, USA
[26]Stanford University, Stanford, CA 94305, USA
[27]IM-PAN 00-956 Warsaw[a]; Astronomical Observatory Warsaw University 00-478 Warsaw[b]; CAMK-PAN 00-716 Warsaw[c]; Białystok University 15-424 Białystok[d]; NCBJ 05-400 Świerk-Otwock[e]; Institute of Astronomy 65-265 Zielona Góra[f], Poland
[28]The University of Texas at Brownsville, Brownsville, TX 78520, USA
[29]San Jose State University, San Jose, CA 95192, USA
[30]Moscow State University, Moscow, 119992, Russia
[31]LAL, Université Paris-Sud, IN2P3/CNRS, F-91898 Orsay[a]; ESPCI, CNRS, F-75005 Paris[b], France
[32]NASA/Goddard Space Flight Center, Greenbelt, MD 20771, USA
[33]University of Western Australia, Crawley, WA 6009, Australia
[34]The Pennsylvania State University, University Park, PA 16802, USA
[35]Université Nice-Sophia-Antipolis, CNRS, Observatoire de la Côte d'Azur, F-06304 Nice[a]; Institut de Physique de Rennes, CNRS, Université de Rennes 1, 35042 Rennes[b], France

[36]Laboratoire des Matériaux Avancés (LMA), IN2P3/CNRS, F-69622 Villeurbanne, Lyon, France

[37]Washington State University, Pullman, WA 99164, USA

[38]INFN, Sezione di Perugia[a]; Università di Perugia[b], I-06123 Perugia; Università di Camerino, Dipartimento di Fisica[c], I-62032 Camerino, Italy

[39]INFN, Sezione di Firenze, I-50019 Sesto Fiorentino[a]; Università degli Studi di Urbino 'Carlo Bo', I-61029 Urbino[b], Italy

[40]University of Oregon, Eugene, OR 97403, USA

[41]Laboratoire Kastler Brossel, ENS, CNRS, UPMC, Université Pierre et Marie Curie, 4 Place Jussieu, F-75005 Paris, France

[42]University of Maryland, College Park, MD 20742 USA

[43]Universitat de les Illes Balears, E-07122 Palma de Mallorca, Spain

[44]University of Massachusetts - Amherst, Amherst, MA 01003, USA

[45]Canadian Institute for Theoretical Astrophysics, University of Toronto, Toronto, Ontario, M5S 3H8, Canada

[46]Tsinghua University, Beijing 100084 China

[47]University of Michigan, Ann Arbor, MI 48109, USA

[48]Louisiana State University, Baton Rouge, LA 70803, USA

[49]The University of Mississippi, University, MS 38677, USA

[50]Charles Sturt University, Wagga Wagga, NSW 2678, Australia

[51]Caltech-CaRT, Pasadena, CA 91125, USA

[52]INFN, Sezione di Genova; I-16146 Genova, Italy

[53]Pusan National University, Busan 609-735, Korea

[54]Australian National University, Canberra, ACT 0200, Australia

[55]Carleton College, Northfield, MN 55057, USA

[56]The University of Melbourne, Parkville, VIC 3010, Australia

[57]INFN, Sezione di Roma Tor Vergata[a]; Università di Roma Tor Vergata, I-00133 Roma[b]; Università dell'Aquila, I-67100 L'Aquila[c], Italy

[58]University of Salerno, I-84084 Fisciano (Salerno), Italy

[59]Instituto Nacional de Pesquisas Espaciais, 12227-010 - São José dos Campos, SP, Brazil

[60]The University of Sheffield, Sheffield S10 2TN, United Kingdom

[61]Wigner RCP, RMKI, H-1121 Budapest, Konkoly Thege Miklós út 29-33, Hungary

[62]Inter-University Centre for Astronomy and Astrophysics, Pune - 411007, India

[63]University of Minnesota, Minneapolis, MN 55455, USA

[64]INFN, Gruppo Collegato di Trento[a] and Università di Trento[b], I-38050 Povo, Trento, Italy; INFN, Sezione di Padova[c] and Università di Padova[d], I-35131 Padova, Italy

[65]California Institute of Technology, Pasadena, CA 91125, USA

[66]Northwestern University, Evanston, IL 60208, USA

[67]Rochester Institute of Technology, Rochester, NY 14623, USA

[68]Eötvös Loránd University, Budapest, 1117 Hungary

[69]University of Cambridge, Cambridge, CB2 1TN, United Kingdom

[70]University of Szeged, 6720 Szeged, Dóm tér 9, Hungary

[71]Rutherford Appleton Laboratory, HSIC, Chilton, Didcot, Oxon OX11 0QX United Kingdom

[72]Embry-Riddle Aeronautical University, Prescott, AZ 86301 USA

[73]Perimeter Institute for Theoretical Physics, Ontario, N2L 2Y5, Canada

[74]American University, Washington, DC 20016, USA

[75]University of New Hampshire, Durham, NH 03824, USA

[76]University of Southampton, Southampton, SO17 1BJ, United Kingdom

[77]Korea Institute of Science and Technology Information, Daejeon 305-806, Korea
[78]Hobart and William Smith Colleges, Geneva, NY 14456, USA
[79]Institute of Applied Physics, Nizhny Novgorod, 603950, Russia
[80]Lund Observatory, Box 43, SE-221 00, Lund, Sweden
[81]Hanyang University, Seoul 133-791, Korea
[82]Seoul National University, Seoul 151-742, Korea
[83]University of Strathclyde, Glasgow, G1 1XQ, United Kingdom
[84]The University of Texas at Austin, Austin, TX 78712, USA
[85]Southern University and A&M College, Baton Rouge, LA 70813, USA
[86]University of Rochester, Rochester, NY 14627, USA
[87]University of Adelaide, Adelaide, SA 5005, Australia
[88]National Institute for Mathematical Sciences, Daejeon 305-390, Korea
[89]Louisiana Tech University, Ruston, LA 71272, USA
[90]McNeese State University, Lake Charles, LA 70609 USA
[91]Andrews University, Berrien Springs, MI 49104 USA
[92]Trinity University, San Antonio, TX 78212, USA
[93]University of Washington, Seattle, WA, 98195-4290, USA
[94]Southeastern Louisiana University, Hammond, LA 70402, USA

E-mail: robinet@lal.in2p3.fr

Abstract.
Between 2007 and 2010 Virgo collected data in coincidence with the LIGO and GEO gravitational-wave (GW) detectors. These data have been searched for GWs emitted by cataclysmic phenomena in the universe, by non-axisymmetric rotating neutron stars or from a stochastic background in the frequency band of the detectors. The sensitivity of GW searches is limited by noise produced by the detector or its environment. It is therefore crucial to characterize the various noise sources in a GW detector. This paper reviews the Virgo detector noise sources, noise propagation, and conversion mechanisms which were identified in the three first Virgo observing runs. In many cases, these investigations allowed us to mitigate noise sources in the detector, or to selectively flag noise events and discard them from the data. We present examples from the joint LIGO-GEO-Virgo GW searches to show how well noise transients and narrow spectral lines have been identified and excluded from the Virgo data. We also discuss how detector characterization can improve the astrophysical reach of gravitational-wave searches.

PACS numbers: 04.80.Nn,95.75.Wx,07.60.Ly,95.55.Ym

1. Motivations

The first-generation gravitational wave (GW) interferometric detectors, TAMA300 [1], LIGO [2], GEO600 [3] and Virgo [4], have performed several GW searches over the last decade. In 2007-2010, LIGO, GEO600 and Virgo detectors operated in coincidence at, or near, their design sensitivities. Many noise events and non-stationarities are present on top of the fundamental Gaussian component of the detector output, and so searches for GW events require signals to be observed in multiple detectors to reduce the large number of false-alarm events due to instrumental or environmental disturbances. A multi-detector network also offers a better sky coverage and the possibility of localizing the source's sky position. The detection of a GW event is expected to be unlikely given the detector sensitivities in 2007-10, and, in the analyses performed so far, no GW signal has been detected by the LIGO-GEO-Virgo network of interferometers.

In GW searches for rare transients, weak continuous signals or a stochastic background, the strain amplitude time series $h(t)$ of each detector may contain a GW signal buried in the instrumental noise. The sensitivity of interferometric detectors varies as the detector noise increases or decreases. Noise events and GW events can have similar properties and the challenge of a data-quality investigation is to discard as many noise events as possible in order to improve the sensitivity of GW searches.

Many astrophysical sources are expected to emit short duration GW signals, such as: the inspiral and coalescence of binary neutron stars and/or black holes [5], core collapse supernovae [6], pulsar glitches [7], newly formed and rapidly spinning neutron stars [8], accreting neutron stars in low-mass X-ray binaries [9], soft gamma repeater giant flares, anomalous X-ray pulsars [10] and cosmic (super)-strings [11]. When the GW signal waveform is well modeled, as in the case of the compact binary coalescence (CBC), template-based matched filtering techniques are used to search for GWs [12, 13]. Otherwise, robust methods to detect a "burst" of excess energy in the detector network are used [14, 15]. Burst detections are particularly susceptible to the presence of transient noise events (or *glitches*). Even matched filtering searches are affected by noise glitches, especially when the templates are of short duration. For these reasons we must understand the nature and the source of the glitches in a detector. However the amplitude distributions of these noise transients do not follow a Gaussian distribution. For many years in Virgo, starting with the first "commissioning" runs, great efforts have been made to identify and locate transient noise sources that couple into the output of the detector. In the best case scenario, provided that a noise source is understood, it is possible to mitigate the noise in the detector or its environment. This paper will provide a few examples of such cases. However, for many transients, the noise source cannot be eliminated or the cause is only understood after the end of the data acquisition period. Therefore there is no choice but to exclude short periods of time surrounding these noise events. We refer to this as "vetoing".

In addition to transient GW signals, continuous gravitational wave (CW) signals are expected to be produced by rapidly-spinning non-axisymmetric neutron stars. A

CW signal is expected to be contained in a narrow band Δf centered on a frequency f_0, which depends on the emission mechanisms at work [16]. Targeted searches for known pulsars [17, 18, 19] (known frequency, position and spin-down rate) use matched filtering techniques and are restricted to a narrow frequency band ($\Delta f \sim 10^{-4} f_0$). The search for CW signals with unknown parameters is performed over a much larger parameter space [20] (all-sky, GW frequencies between 20 Hz and 2 kHz, and for several possible values of the spin-down rate) which reduces the sensitivity of the search. Broad-band increases of the detector noise level are the first obstacle for CW searches [21]. This paper, however, focuses on narrow-band frequency disturbances called spectral lines (or lines). The presence of lines in the detector frequency spectrum can significantly reduce the sensitivity of CW searches. The origins of several lines in the Virgo sensitivity curve (figure 2) are well-known. Some of these lines are associated with resonances of different detector components, including the mirrors ("drum modes") or the suspension wires ("violin modes"). This family of lines is part of the detector design and cannot be removed from the data. There are also constant frequency signals which are injected into the detector for calibration and control purposes. This paper focuses on a second class of lines which are more problematic since many of them have no identified origin or they cannot be mitigated easily without degrading the general performance of the detector. Furthermore, some of these noise lines are not stationary; they fluctuate in amplitude and frequency, making their identification more complicated. These non-stationarities can also be a source of glitches that affect transient GW searches. It is thus important to track the noise spectral lines, to monitor their characteristics (frequency, amplitude and variability) to ensure that they do not cross the frequency band of a known pulsar. Both LIGO and Virgo have dedicated data-analysis tools to achieve this task and to help identify the sources of noise lines [22, 23, 24, 25].

A stochastic gravitational wave background (SGWB) is expected to be emitted in the early stages of the universe evolution (by inflation [26], electroweak phase transition [27] and cosmic strings [28]) or produced as a consequence of the incoherent superposition of many astrophysical sources like core collapse supernovae [29], magnetars [30] or neutron star coalescence [31]. SGWB searches correlate two detector's strains over a wide frequency range [32, 33] and are also affected by noise spectral lines. The SGWB search is also sensitive to large transients which distort the estimation of the detector frequency spectrum used to measure the signal. The published SGWB search involving Virgo [34] made use of the data-quality work described here for transient searches to reject the most noisy time periods for the analysis.

This paper gives an overview of the data-quality studies carried out during the three Virgo science runs designated as VSR1, VSR2 and VSR3 which occurred during 2007-2010 (see table1). Many noise sources were identified by our investigations and we describe the actions taken to mitigate noise or the procedure used to veto remaining noise events. The paper is organized as follows: section 2 presents the Virgo detector, its sensitivity to GWs and the different Virgo data-taking campaigns over the years. Several detector sub-systems are also briefly described. In section 3, a summary of the

detector characterization work is given. Section 4 focuses on transient noise sources. We present the different methods which have been developed to identify glitches, we list the noise sources which have been identified and we explain how they couple with the strain output. This section also describes the actions to remove glitches either at the detector level or from the data-analysis, with the definition of data quality flags. Noise spectral lines, which primarily affect CW and SGWB searches, are discussed in section 5. Methods for identifying lines are briefly described and we review the main families of lines. Finally, section 6 shows how the Virgo detector characterization work impacts the transient GW and CW searches involving Virgo data. We conclude with section 7, where we present ideas for improvement of the detector characterization tools and procedures for the next generation of GW detectors.

2. The Virgo Detector

Virgo is an interferometric GW detector located near Pisa, Italy, aiming at directly observing GWs. The optical layout of the detector is based on a power-recycled Michelson interferometer where each arm contains a 3-km long Fabry-Perot cavity. The Virgo experiment layout is shown on figure 1. An incident GW from a plausible astrophysical source induces a differential length variation (smaller than 10^{-18} m) between the test masses suspended at both arm ends. The interferometer is set to operate at a dark fringe and photo-diodes at the output of the interferometer observe a GW signal as a fluctuation in the intensity of the light. In the following we will often refer to the dark fringe (DF) as the uncalibrated GW detection channel. The calibrated GW strain amplitude, $h(t)$, is reconstructed taking into account the frequency-dependent transfer functions of the instrument [35, 36] which are applied to the DF signal. The ability to detect GWs relies on the stability of the detector, and much attention is given to critical systems of the instrument: the mirrors, laser and feedback controls.

The isolation of the test masses from seismic activity is crucial in order to ensure good sensitivity, especially at low frequencies. In Virgo, sophisticated super-attenuators (SA) [37] have been installed to decouple mirror motion from seismic fluctuations. A SA consists of an eight meter chain of five mechanical pendula with a connection to the ground by three elastic legs, playing the role of an inverse pendulum. The bottom part of the suspension, called the payload, is composed of mechanical elements that suspend the mirror and control its motions. This payload is suspended from the last stage of the SA. The SA allows for good sensitivity down to 10 Hz.

The main laser (a 1064 nm Nd:YaG laser [38]) is a critical component of the interferometer and special attention must be given to its stability and its operation. The laser frequency and power are stabilized and the laser position jitter is controlled to limit the impact of environmental disturbances [39]. A suspended 144 m triangular cavity, called the Input Mode Cleaner (IMC), is used to remove high-order modes from the light. The laser propagation takes place inside a high-quality vacuum to limit air contamination which could induce phase noise. Scattered light represents a major
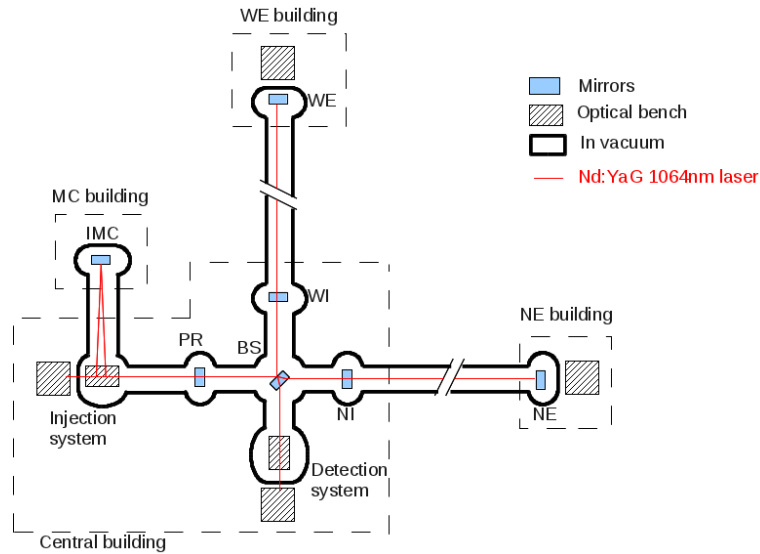
Figure 1. The Virgo detector layout showing the main laser path through the input mode cleaner (IMC), the power recycling mirror (PR), the beam splitter (BS), the western cavity (WI-WE), the northern cavity (NI-NE) and the detection system. Most of the laser propagation is performed in high-vacuum [4].

contribution to the Virgo noise since it can recombine with the main laser beam. Such an effect is limited by installing beam dumps and baffles at strategic points inside the vacuum tanks [40].

The optical cavities are maintained at resonance using the Pound-Drever-Hall technique [41], relying on a laser beam phase-modulated at 6.26 MHz. DC and demodulated signals from different photo-diodes throughout the detector are used to control the interferometer. The control loops, running at a sample rate of 10 kHz, are composed of Analog to Digital Converters (ADC), and a real-time software architecture that is used to reconstruct the cavities length. The control system also sends corrections to the mirror actuators (coils in front of magnets) through Digital to Analog Converters (DAC) to keep the optical cavities resonant. Special care is taken to keep the electronic noise at a very low level and to insure a reliable synchronization between the different control processes involved in the feedback systems [42, 43].

Virgo can detect GWs with an amplitude as low as 10^{-21} over a wide frequency band, from tens to thousands of hertz (and below 10^{-22} at a few hundreds of hertz). The sensitivity curves shown in figure 2(b) are limited by several types of noise that can be divided into three frequency regions. At low frequencies (below 100 Hz), the sensitivity is limited by mirror and suspension thermal noise, mirror control noises, and environmental noises. Mirror control noise refers to the noise introduced by the feedback systems used to maintain the interferometer alignment and resonance. This noise originates from the actuators' electronics and from the control system's error signals. Environmental noise includes seismic and acoustic disturbances coupling into the interferometer through scattered light or input beam jitter, as well as magnetic
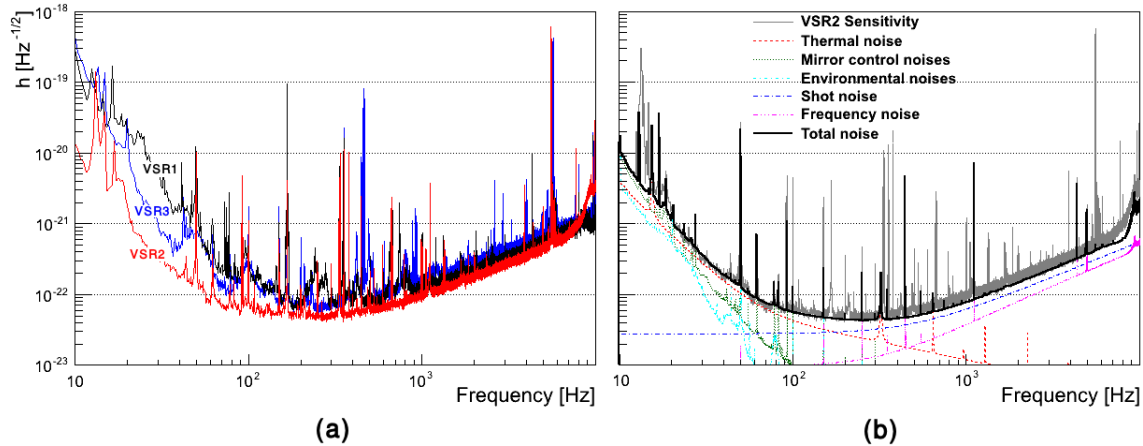
Figure 2. (a) Typical sensitivity vs. frequency curves for the first three Virgo science runs: VSR1 (2007), VSR2 (2009) and VSR3 (2010). (b) The measured VSR2 sensitivity curve is compared to the predicted noise budget [44]. The agreement between the measured and the predicted sensitivity was the best for VSR2. For VSR1&3 the agreement was not as good, especially at low frequency.

disturbances coupling through the mirror magnets. At high frequencies (above 300 Hz) the sensitivity is primarily limited by the shot noise of the main laser beam and by laser frequency noise. The frequency noise originates from the shot noise of the sensor delivering the error signal used in the laser frequency stabilization. For intermediate frequencies (between 100 Hz and 300 Hz), both thermal noise and shot noise limit the sensitivity. Noise structures around 165 Hz and 210 Hz are suspected to originate from scattered light (see section 4.2.6).

In addition to achieving a good sensitivity, it is also important to maintain the detector in operation as long as possible in order to maximize the live-time (or duty cycle). A lock acquisition scheme [42, 43] was designed to bring and maintain the Virgo detector to its working point. The Virgo locking procedure has proved to be very efficient and robust. The lock can last for several hours or days at a time (see table 1). If lock is lost, it can be recovered in a few minutes. When locked, the detector is manually set in science mode when a stable state is reached. When in science mode, no external input or detector tuning is allowed. Science mode ends when decided by the detector operator (for maintenance or tuning) or whenever an instability causes loss of lock of the interferometer. The beginning and the end of a lock segment are considered unsafe in terms of data quality. Thus, the first 300 seconds after the end of locking procedure and the 10 seconds of data before the loss of lock are, *a priori*, rejected and not used for science analysis.

The first Virgo science run, VSR1, took place between May and October 2007, in coincidence with the LIGO detectors. The second run, VSR2, started in July 2009 after a commissioning period devoted to detector upgrades. These upgrades included: more powerful and less noisy read-out and control electronics, a new laser amplifier that provided an increase of the laser power from 17 to 25 W at the input port of

Virgo Science Runs	VSR1	VSR2	VSR3
Date	May 18, 2007 → Oct 01, 2007	Jul 07, 2009 → Jan 08, 2010	Aug 14, 2010 → Oct 20, 2010
Duty cycle (% of lock time)	81%	80%	73%
Science time	108 days	149 days	50 days
Average lock duration	10 hours	10 hours	9 hours
Max lock duration	94 hours	143 hours	63 hours
Omega average trigger rate (SNR > 5)	2.1 Hz	0.6 Hz	1.8 Hz

Table 1. Virgo runs summary information. Omega [45] triggers are generated online to estimate the rate of transient noise events.

the interferometer, and the installation of a thermal compensation system (TCS) [46], to reduce the effects of thermal lensing in the arms' input mirrors. As a result, the detector sensitivity was much improved with respect to the previous run, as can be seen on figure 2(a). VSR2 lasted six months, after which further upgrades were performed. Higher reflectivity mirrors were installed to increase the finesse of the Fabry-Perot cavities. As a test for Advanced Virgo [47], these mirrors were hung by a new suspension made of monolithic silica-fibers in order to reduce thermal noise effects [48]. These detector upgrades took six months before resuming science with VSR3 from August to October 2010. The resulting sensitivity in VSR3 was not as good as expected, however, and was slightly worse than VSR2. It was not possible to obtain a reliable noise budget in VSR3. It was discovered that the newly-installed mirrors had a large asymmetry in the radius-of-curvature and losses. This increased the interferometer's contrast defect, resulting in higher power in the DF and stronger couplings to some noise sources. This paper focuses on the detector characterization work performed during the three first Virgo science runs. A final run, VSR4, occurred in 2011 for which very few references will be given in the following. Table 1 summarizes the performance of the Virgo science runs covered in this paper.

3. Detector characterization

The power spectral density shown in figure 2 is an incomplete representation of detector performance as it does not include transient effects which reduce the sensitivity of GW searches. The DF signal can be disturbed by a large variety of noise sources originating from within the detector or from its environment. The noise path (or coupling), which connects the noise source to the DF affects the characteristics of the noise. A long process called "noise hunting" consists of tracking down each noise source and understanding the conversion mechanisms which occur between the source and the DF. To achieve this task, the Virgo detector is equipped with hundreds of sensors, including microphones, seismometers, magnetometers, photo-diodes, current and voltage monitors, thermometers and cameras. The signals from these auxiliary channels are used to monitor external disturbances to help determine whether a candidate event found by a search pipeline was produced by a GW or by an instrumental

artifact. The Virgo noise hunting process can be summarized as the following:

 (i) Identify events (glitches or noise spectral lines), or a family of events with similar properties, seen in the DF.

 (ii) Correlate this event with some unusual detector behavior or environmental disturbances (human intrusions, earthquakes, thunderstorms, etc.).

(iii) Check the event time against external scheduled events, such as the stop/start of infrastructure machineries or changes in the interferometer running configuration.

(iv) An extensive study is performed to tell whether the event occurred in time coincidence with an event in one or several auxiliary channels. Statistical algorithms are used to quantify the correlations between auxiliary channels and the DF, see sections 4.3 and 5.1 for more details.

 (v) In many cases, the previous studies cannot differentiate whether the noise has been identified at its source or somewhere along its propagation. Experiments are performed to understand how the noise couples into the DF signal. For example, one can artificially inject noise in a hardware component and study the response of the detector [49]. Another possibility is to switch off a potential noise source to see if the noise disappears. Some examples of such actions are given in sections 4.2 and 5.2.

(vi) If a noise source is identified, the strategy to remove it from the DF is twofold: first we try to eliminate or reduce the noise sources; second, we try to reduce the coupling to the DF.

An important aspect of detector characterization is reaction time. When a problem occurs while Virgo is acquiring data, if we can understand the source of noise quickly, we can make appropriate modifications to the detector or its environment to mitigate the noise. To this end, many algorithms are run online which monitor the detector's data quality. The strain signal is analyzed by various search pipelines to characterize the type of events that limit the sensitivity of the searches. Auxiliary signals are monitored in quasi-real time so as to be able to tell if they are linked to events found in the GW searches. The loudest glitches and noise spectral lines are studied, common features are searched for, and cause-effect relationships are investigated. For VSR2 and VSR3, data was analyzed shortly after it was collected so the commisioning groups could mitigate the noise source/coupling as quickly as possible. Depending on the noise complexity, mitigation actions could last from a few hours to a few days. Interactions between analysis and commissioning groups are imperative to make the noise hunting process efficient.

Because many noise sources cannot be clearly understood or mitigated, they must be identified and tagged in the data. These events will be vetoed when data are processed by search pipelines with data quality flags.

For transient searches, data quality investigations consist of defining lists of time segments of a few seconds long (commonly called DQ flag segments) where there is a high

probability that a glitch is caused by an instrumental or environmental source. A DQ flag is usually defined by using an auxiliary signal that indicates that the interferometer was out of its proper operating condition or that an external disturbance was present. Any event found during flagged times by the data analysis pipelines are vetoed [50, 51, 52] (see section 4.3).

For CW searches, data quality investigations consists of tagging, characterizing and tracking noise spectral lines. Algorithms are used to establish coincidences between lines in the detector output and auxiliary channel signals. This information is then used by the search to reduce the number of false CW candidates (see 5 and 6.2).

All of the data quality information is stored in databases [53, 54]. In addition to reliably archiving data, the Virgo database may also be used to perform specific queries. DQ flags and noise lines can be retrieved by analysis pipelines or through a web interface.

4. Transient noise sources

4.1. Investigations

In Virgo, two analysis pipelines are run online, Omega [45] and MBTA [55], which monitor the data quality for transient GW searches in quasi-real time. Omega is a burst search algorithm which produces triggers based on a sine-Gaussian excess power method with frequencies between 48 and 2048 Hz. A discrete Q transform is applied which consists in tiling the time-frequency plane for a specific quality factor value. For each tile, it is possible to define a central time, a central frequency, a duration and a signal-to-noise ratio (SNR) which is simply the ratio of the total energy content of the tile to the power spectral density of the detector noise. The Omega algorithm is generic enough to produce triggers which are a reliable representation of the output of any transient GW search. Omega is sensitive to typical detector glitches and provides useful information about the glitch properties. Omega triggers are often the starting point for glitch investigation, and special attention is given to high-SNR events. The noise coupling associated with loud events is expected to be more obvious, and therefore easier to understand. Moreover, mitigating or vetoing loud noise events should also remove quieter glitches which are due to the same noise source. The MBTA pipeline was specifically designed to detect GWs associated with the coalescence of compact binary objects. An inspiral waveform template bank is used to match-filter the data. The intercorrelation between the data and the template, weighted with the inverse of the noise power spectral density, defines the event SNR. The glitches detected by the MBTA pipeline are not as generic as the ones produced by Omega since these glitches mimic the specific properties of a CBC signal. However, MBTA triggers give a reasonable sample of the type of glitches that may affect CBC searches.

A glitch detected by Omega or MBTA often results from a sudden environmental perturbation that then propagates through the detector, reaches one of the Virgo sub-

systems sensitive to this kind of perturbation, and then couples to the DF signal. For example, an acoustic disturbance can be converted into mechanical vibrations which can, in turn, affect optical elements or disturb the main laser propagation. Auxiliary channels are constantly monitored and analyses are performed to establish the correlations between glitches in the auxiliary channels and triggers produced by Omega or MBTA (glitch-to-glitch identification). In this way, the most relevant channels are identified, the noise path may be reconstructed, and the noise sources identified.

Some glitches detected by Omega or MBTA can result from a spectral line in the DF which becomes non-stationary in amplitude or in frequency because of fluctuations in the coupling to the noise source (for instance, alignment fluctuations). This effect can be particularly harmful for searches using data whitening procedures (normalization by the detector frequency spectrum) since they amplify slight amplitude variations of spectral lines. For this type of noise, a glitch-to-glitch coincidence with auxiliary signals does not normally identify the coupling and allow us to construct a DQ flag. However, the frequency of the line can help identify the noise source and hence the coupling.

One additional functionality of Omega is its ability to scan a large number of channels and plot the excess energy as a function of time and frequency [45]. This represents a powerful tool to identify families of glitches based on the common patterns of the time-frequency map. Since this process is computationally expensive, it is typically performed only for the strongest glitches or for a particular class under investigation. When establishing the coincidences between channels, it is then possible to reconstruct the noise path for a given family. Figure 3 shows an example of Omega scans of six well-identified families of glitches. For five of these families, a glitch seen in an auxiliary channel allowed us to identify the coupling between the noise and the DF signal.

Most of the detector characterization tools, like Omega scans, were designed to study glitches resulting from linear couplings between the noise source and the DF. Within this framework, a noise source can be identified only if it produces a glitch somewhere on the noise path that could be detected in an auxiliary channel. For example, the scattered-light glitches shown in figure 3 do not trigger other auxiliary channels. Understanding a noise source outside this glitch-to-glitch description is a much harder task. Non-linear couplings are believed to play a major role in the production of noise in the detector. Only a few of these non-linear noise processes have been identified and this requires a deep understanding of the experimental details of the interferometer. Some non-linear couplings will be described in section 4.2.

4.2. Glitch sources and couplings

4.2.1. Seismic glitches.   Seismic activity is probably the most pervasive source of noise in Virgo, affecting the detector in many different ways. Almost every Virgo sub-system is sensitive to sufficiently large vibrations. Seismic noise can produce a large variety of glitches which are very difficult to track. Loud seismic glitches due to violent shocks or earthquakes are likely to produce noise in the DF. If this happens, the data recorded
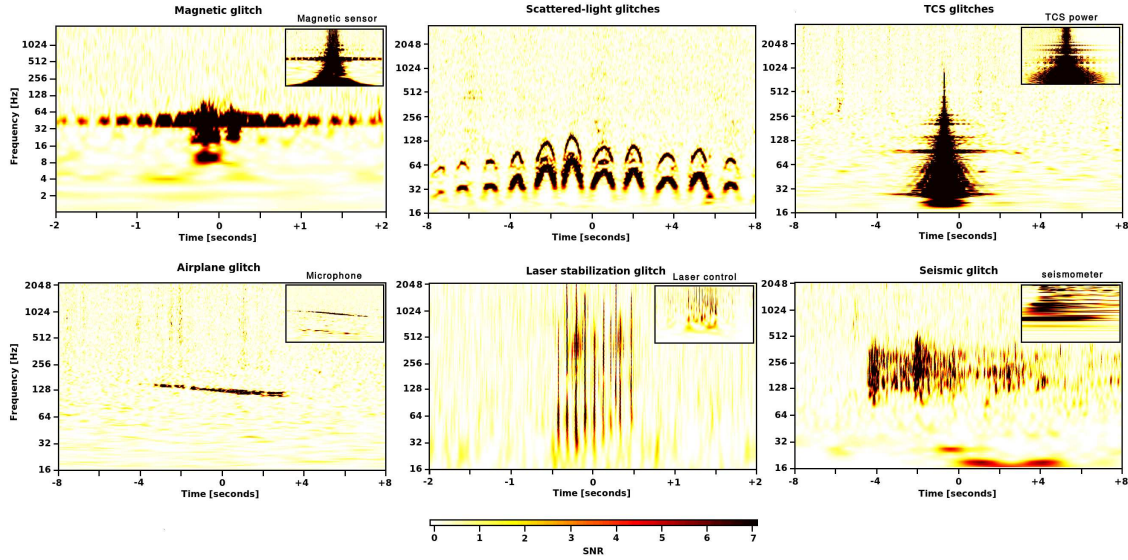
Figure 3. Omega time-frequency maps of six examples of glitches seen in the DF channel. Glitch families are identifiable by their unique time-frequency morphology. When identified, the glitch in the auxiliary channel is shown in the inset plot. The first plot shows a 50 Hz power-line glitch also detected by the magnetometers. The second map shows a series of glitches caused by scattered light induced by seismic activity. The third glitch is caused by a TCS instability. The fourth plot presents an airplane event with a clear Doppler effect. The fifth event is due to a glitch in the laser stabilization loop. The last glitch with an undefined shape is due to a seismic event up-converted to higher frequencies.

during a seismic event is rejected and so the noise coupling is less relevant. The low frequency signals collected by the multiple seismometers and accelerometers on site are used to define DQ flags for large seismic activity. Several frequency bands are monitored at all times, from 0.25 Hz up to 16 Hz. *A priori*, such low-frequency seismic glitches should not be an obstacle for the transient GW searches whose frequency band usually starts above 40 Hz. However, seismic noise is often up-converted in frequency, for example through scattered light mechanisms as described in [56]. For example, the seismic glitch presented in figure 3 was detected by the seismometers at about 8 Hz and is seen in the DF signal at much higher frequency (~ 200 Hz).

Bad weather conditions can increase the seismic activity and cause significantly deteriorated data quality. In such conditions, the Omega pipeline shows an excess of triggers at low frequency (typically below 100 Hz). In the case of very bad weather, the Omega trigger rate below 100 Hz can increase by a factor 5 to 7. During the winter, VSR2 showed many periods of high seismic noise. Substantial efforts were devoted to studying the resulting glitches [56]. One family of scattered-light glitches was characterized by no visible glitch in the Omega time-frequency maps of the seismic sensors. This fact indicates that a non-linear coupling was in action. The time-frequency shape of these triggers is very well-recognizable (see the second plot of figure 3). It consists of a series of arch-shaped glitches that can last several seconds. The glitches

are caused by light scattered by e.g. the tower walls or the suspended baffles moving with the micro-seismic motion of the ground. When the micro-seismic activity is large, higher harmonics can be seen, probably due to multiple-bounce optical paths. In such conditions, several rows of arch-shaped glitches can be seen in time-frequency maps. This noise is well-modeled and the frequency of the arches is proportional to the velocity of the scattering object. Tests showed that the position sensors installed at the top stage of the suspensions are well suited to measure the velocity. The scattered-light glitches can be rejected when thresholding on the measured velocity. When applying the DQ flag created in this way, 8% of the science time is lost but 2/3 of the scattered-light glitches were vetoed. The coupling mechanism for the scattered-light glitches was understood during VSR2 when it was noticed that most of the scattered light was re-injected into the beam at the level of the west-end optical bench. For VSR3 the number of scattered light glitches decreased because of the lower transmission of the new end mirrors and the installation of absorbing baffles in the west-end tube.

4.2.2. Acoustic glitches. Acoustic disturbances can mechanically affect the Virgo systems and produce glitches. Acoustically-isolating enclosures have been installed around each optical bench in order to limit the acoustic coupling with the environment. However, acoustic pollution can either be produced inside the enclosure or can get inside through mechanical vibrations. To monitor acoustic noise, each building is equipped with several microphones. Most of the time, the acoustic disturbances originate from mechanical devices located near the interferometer which can be mitigated. However, acoustic noise can also have an external origin which cannot be controlled or suppressed. Several times during the day, airplanes or helicopters fly over Virgo and they are seen in the DF signal. These glitches can be clearly identified by the typical Doppler shift at about 100 Hz seen in time-frequency maps of the detector output (see an example in figure 3) [57].

4.2.3. Electrical glitches. Electrical cables represent a major source of noise coupling since they can propagate an electrical disturbance throughout the Virgo site. The Virgo sub-systems are usually designed to be electrically isolated from the environment. However the 50 Hz mains frequency (European standard) can couple into the detector and transmit magnetic transients. For example, during VSR2, it was noticed that a family of glitches was periodically produced roughly every 15 minutes. This effect was identified as electrical coupling of an air-conditioning unit switching on and off. During the winter period of VSR2 a loud glitch was produced every day at 8am due to the heating system that switched on at the beginning of the day and drew a significant amount of current. Such glitches can be vetoed by using magnetic sensors that are sensitive to electrical transients. Electrical glitches are usually corrected by breaking the electrical noise path. In the two specific cases here, the glitches disappeared after upgrades to the detector electronics.

4.2.4. Main laser glitches. One critical element of the Virgo detector is the main laser injection system. This system contains many control loops to stabilize the laser power and frequency. Failures in these control systems caused various families of glitches. During VSR3, the laser power stabilization control loop was experiencing saturations due to a mis-tuned gain. This created strong broadband glitches from tens to thousands of Hz (see figure 3). This was fixed a few days after the problem was discovered. In the meantime a specific DQ flag was built to monitor the control loop channel and to efficiently exclude the glitches from the data attributed to the control failure.

4.2.5. Dust glitches. Most of the laser light propagation is done in a high-quality vacuum. However the beam propagates through air in some parts of the detector, for instance on the injection and detection benches. Some disturbances, due to dust crossing the beam, for example, create glitches which are difficult to veto. The laser light propagation can also be disturbed by unexpected events like spiders building webs or bugs flying through the beam. It is possible to limit such pollution by protecting the laser path with plastic covers. Some of the remaining glitches can be vetoed by using the photo-diode signals of the secondary beams which are not sensitive to GW signals. Many DQ flags were created in this way. A very efficient veto was introduced in VSR1 which relies on the fact that a real GW event seen in the in-phase demodulated DF channel should not be visible in the quadrature channel if the demodulated phase is well-tuned. This PQ veto [58] has been extensively used to eliminate these potential "dust events" in the Virgo data.

4.2.6. Alignment glitches. The alignment of the main optical beam is critical in order to maintain the detector in operation. Sophisticated feedback systems are required to continuously control the optical component angular degrees of freedom and to optimize the laser beam alignment [59, 60]. In the Virgo sensitivity curves shown in figure 2(a) several spectral lines are known to correspond with resonances of some optical mounts of the detection bench (165, 210, 420, 495 and 840 Hz) and are due to light scattered by these optical components. In principle they should not be seen as glitches unless they suddenly vary in amplitude which can happen when the interoferometer alignment conditions change. This effect of non-stationary lines is a well-known source of glitches to which transient GW searches are very sensitive. In Virgo, alignment glitches represent a quite large fraction of Omega triggers (about 25%). In the case of bad weather, alignment fluctuations are even larger. As a result, the fraction of glitches due to alignment reaches 40% and the amplitude of the glitches increases. Alignment signals can be used to build DQ flags to suppress these alignment glitches. For VSR2 and VSR3, large deviations of the mirror angular positions were flagged. This allowed for the removal of as much as half of the alignment glitches.

4.2.7. TCS glitches. The thermal compensation system [46] was installed in Virgo between VSR1 and VSR2. A TCS instability can directly influence the DF signal by

producing a thermal or a radiation pressure disturbance at the mirror level. During VSR2, the TCS laser has been stabilized, reducing the number of glitches. However, it was necessary to build a specific DQ flag, using the channel monitoring the TCS power, to veto the remaining glitches. Figure 3 shows an example of a TCS glitch that is vetoed by a DQ flag.

4.2.8. Saturation glitches. Very loud glitches can be produced by the saturation of different Virgo active systems. For instance, every photo-diode must operate within its nominal range (±10 V). Specific DQ flags have been introduced to reject noise transients whenever a photo-diode voltage is out-of-range. Similarly, the mirror coil driver currents are monitored to check for saturations.

4.2.9. Tilt glitches. In data taken two years before the first science run, we identified a non-linear coupling between the dark fringe and the laser frequency noise. Laser frequency noise usually lies well below the shot noise level at high frequencies (see figure 2(b)). Every 27 s, broadband glitches were visible in the DF signal. This period corresponds to a mechanical resonance in the lower part of the mirror suspension. The periodic noise increase was correlated with the extremal angular tilt of the Fabry-Perot cavity's mirrors. When the mirrors are badly aligned the coupling of the laser frequency noise increases. To cure this problem, the mirrors' alignment control loops have been greatly improved. A veto using the direct measurement of the laser frequency noise in the DF signal (a line at 1111 Hz was injected in the laser frequency control system) was created to efficiently eliminate all of the periods containing this noise [61].

4.2.10. Piezo glitches. The Virgo detector has many piezo-electric drivers used to control various elements of the beam path. At the beginning of VSR1, one of the four piezos of the beam monitoring system was malfunctioning, causing the input beam to jitter [62]. This jitter can couple to interferometer asymmetries and was a source of glitches in the DF signal. The typical frequency of theses glitches was around 150 Hz. This problem was discovered during the first month of the run and the piezo was replaced two months later. A similar problem occurred during VSR3 at the output mode cleaner. A piezo voltage was found noisy for several hours. The faulty piezo elements were fixed but DQ flags, based on the control channels, were defined in order to completely exclude the glitches from the data recorded while the piezo was faulty.

4.2.11. Mirror glitches. During VSR2, some glitches were observed with the distinctive feature of an abrupt step in the $h(t)$ time series which resulted in a loud broadband disturbance. Theses glitches were demonstrated to be associated with an excitation of the internal modes of the west-input (WI) or west-end (WE) mirrors (depending on the glitches), identified by their accurately known frequencies. The glitches were interpreted as a sudden displacement of the surface of those mirrors, of unknown origin. In the case of the WI mirror, the glitches appeared after the magnets glued on the back

of the mirror were replaced using a type of glue that had not been used before for that purpose, suggesting the possibility of a creeping mechanism in the hygroscopic glue. It was not possible to firmly confirm this suspicion, and the cause of the WE mirror noise still lacks a convincing explanation. It was impossible to safely veto those glitches, due to the lack of independent auxiliary information.

4.2.12. Thermo-mechanical glitches.   The external temperature can also be an indirect source of glitches. The steel vacuum tubes, in which the laser travels, have poor thermal isolation. Hence, external temperature variations are very likely to mechanically stress the tube through contraction and expansion. During VSR4, it was understood that when the expansion/contraction force exceeds the static friction which holds the tube on its support, a sudden shock occurs and a mechanical vibration propagates along the tube. This effect is the strongest around noon and midnight when the temperature gradient is the largest. Seismometers have been installed to track the noise propagation and it was found that the noise source was the tube between the IMC and the injection tower. The resulting glitches are produced in the DF signal at about 80 and 160 Hz. A seismometer placed on the injection tower allowed us to flag these glitches with high efficiency.

4.2.13. Radio frequency glitches. High-frequency electromagnetic noise overlapping with the laser modulation frequency (6.26 MHz) can be picked up by the DF photodiode signal before demodulation. It can then enter the detector's sensitive band after demodulation. High-frequency electromagnetic transients are generated, for example, by fast switching electronic devices (i.e. power supplies with a typical switching rate of 100 kHz and above), and by data flow to/from digital devices (the clock rate of communication protocols is typically in the MHz range). During VSR2 the 6.26 MHz modulation signal was intermittently polluted by a large amount of glitches that were also seen in the DF signal. The origin of this noise has never been identified, mostly because of its intermittent nature. The noise was suspected to originate from serial transmission devices. It was possible to build a DQ flag based on the modulation signal to remove the glitches seen in the DF signal. The beginning of VSR3 showed a large excess of Omega glitches at high frequency (at 1 kHz and beyond). This was identified as a result of a coupling between the modulated DF signal and an electromagnetic field whose frequency was close to the modulation frequency (see section 5.2.2 for more details).

4.2.14. Digital glitches.   The Virgo interferometer is kept at its working point by various digital control loops. The control servos dedicated to longitudinal control are fast control loops running at 10 kHz and any digital problem occurring in theses systems can directly affect the DF signal. One example is a set of loud glitches in VSR1 that were due to a loss of synchronization in the control system. This led to dropped samples between the global control system (which provides the 10 kHz signals for the interferometer's

longitudinal control) and the Digital Signal Processing board in charge of filtering the correction signal before it is sent to a mirror's coil. Combined with a strong but harmless 5 kHz oscillation that is sometimes present in the control signals, the dropped samples produced loud glitches which were vetoed offline by searching for missing samples within the 5 kHz noisy time periods.

4.3. Data quality flagging

In the previous section, the sources of transient noise, which were identified during the first three Virgo science runs, were listed. As the sources were understood and localized, the commissioning team tried to fix the noise sources when possible. However, it was necessary to create a dedicated DQ flag to veto the glitches before the fix was performed or when a repair was impossible.

As explained previously, some DQ flags were created by monitoring a given set of auxiliary channels indicative of noise perturbations (seismic, acoustic, etc.). The same procedure is used for many DQ flags: it consists of computing the frequency spectrum of a given auxiliary channel and to extract the RMS in a specific frequency band (band-RMS). If this RMS exceeds a given threshold, the data are flagged as noisy. Many generic seismic flags are generated online in such a fashion. About 30 seismic sensors are monitored in different frequency bands: 0.25-1 Hz for the weather conditions, 1-4 Hz for the car traffic activity and 4-16 Hz for the human activity. Acoustic and magnetic disturbances are monitored the same way. This kind of environmental DQ flag does not necessarily point toward a glitch in $h(t)$ but corresponds to a weaker statement: "an environmental disturbance was present in the vicinity of the detector".

When the noise path to the DF has been understood, it is possible to use more specific procedures to create a DQ flag that deals with a category of glitches and which has a great predictive behavior (measured by the use-percentage defined in section 4.3.2). In other words, when a time period is flagged the probability to find a glitch in the GW data has to be high. A good DQ flag has to be selective but also efficient (it must not miss too many glitches of the same class). Section 4.2 gives many examples of DQ flags created to veto specific glitches. Sometimes these flags rely on a band-RMS where the parameters have to be carefully tuned. In some cases a simple threshold on the channel value is enough to give good flag performance. There are also some examples where DQ flags had to be specifically tailored for a given family of glitches. In section 4.2.1 we gave the example of the scattered-light glitches where the velocity of the scatterer was used to create the flag. Sometimes it is necessary to combine several channels. One example of this was the DQ flag created to monitor glitches produced by the large angular deviations of the mirrors (section 4.2.6). Multiple mirror degrees of freedom had to be combined to produce an effective DQ flag. Finally, in some cases, it has been necessary to use several channels in time coincidence to provide a DQ flag with good selection abilities. For instance the 50 Hz glitches, detailed in section 4.2, are usually seen all over the Virgo site in the magnetic sensors. Therefore the corresponding DQ

flag is defined as a time coincidence between the band-RMS excesses obtained from several auxiliary signals.

Another method to perform glitch flagging relies on a statistical approach and does not require any knowledge about the noise source or the coupling. In this method, we systematically look for noise excess in many auxiliary channels and correlate it with glitches in the GW data. For this purpose, the KleineWelle (KW) algorithm [63] is used to produce triggers for more than 500 Virgo auxiliary channels with a very low latency. As for Omega, the KW algorithm searches for a statistically significant excess of power in the time-frequency plane but it relies on a wavelet transform instead of a Q transform. Omega is known to better estimate the trigger parameters like the frequency or the SNR. However, Omega runs much slower than KW which explains why KW was chosen to perform the auxiliary data analysis. KW triggers are then used by algorithms such as use-percentage veto (UPV) [64] or hierarchical Veto (hVeto) [65] to establish coincidences between triggers of a given auxiliary channel and GW triggers. When the number of coincidences is much larger than the expected rate of random coincidences, the channel is selected as interesting in order to define a powerful veto. By construction, a KW-based veto does not result from an understood coupling mechanism. For this reason, this type of vetoes are considered less reliable. This statistical approach is not only good in terms of glitch flagging but it can also be a great tool for the glitch investigation. By identifying the auxiliary channel that best correlates with the DF, this method can help understand the origin of glitches. In this case, the KW-based veto was used to construct a DQ flag using a band-RMS of the channel of interest.

Finally, some DQ flags are defined manually by the scientist on shift in the Virgo control room or at a later time. These DQ flags often refer to serious detector malfunctions or disturbances in detector operation. Thunderstorms or earthquakes are systematically reported and the corresponding time segments are saved for future reference. The detector operation logbook [66] is also carefully examined and when a Virgo sub-system failure is reported, a specific DQ flag is created. For example, several DQ flags were defined based on photo-diode, TCS or data-acquisition malfunctions.

In the following, all flags and vetoes described above, including the PQ veto, are called DQ flags. When designing a DQ flag, one should always keep in mind that the flag must not couple to a real GW event (i.e. the flag is safe for the GW events), while, at the same time, it must efficiently eliminate noise transients (the flag has good performance). Those two important aspects are described in the next two sections.

4.3.1. Data quality flag safety. All vetoes, except the PQ veto [58], are derived from channels that are assumed to be independent of the DF (which may contain a GW signal). By accident, a veto can dismiss a genuine GW signal, but the probability of such an event must be small and follow the Poisson probability of coincidence between two random processes. To test that a veto is safe, fake GW signals are injected into the interferometer by applying a force on one mirror of one Fabry-Perot cavity to mimic the path of a GW event (hardware injections). Different types of signals are injected, but

to test the veto safety, the very loud (SNR ~ 100) GW burst signals were used (Sine Gaussian waveforms with a frequency between 50 Hz and 1300 Hz). These hardware injections, grouped by 10, are regularly performed at a rate that varies between once a day and once each three days, depending on the science run. We count the number $N_{flagged}$ of vetoed hardware injections. This number is compared to the expected number of hardware injections accidentally vetoed:

$$N_{flagged}^{exp} = \frac{T_f}{T_{tot}} \times N_{GW} \ , \tag{1}$$

where T_f is the time rejected by the flag, T_{tot} is the total science time and N_{GW} is total number of hardware injections performed during T_{tot}. The Poisson probability to have $N_{flagged}$ or more events when $N_{flagged}^{exp}$ are expected is simply

$$p(N \geq N_{flagged}) = \sum_{n=N_{flagged}}^{n=\infty} P(n, N_{flagged}^{exp}) \ , \tag{2}$$

where $P(n, \lambda)$ is the Poisson distribution of mean λ. This defines the probability that the veto is safe. Setting a threshold on this quantity provides an automatic means to determine which veto is unsafe. Two thresholds were considered: when the probability is lower than 10^{-5}, the flag is considered unsafe. When the probability is below 10^{-3}, all flagged hardware injections are manually inspected to determine if this low probability is due to the fact that a long DQ flag segment has vetoed several hardware injections belonging to the same series since the hardware injections are grouped by 10, each separated by 5 seconds. It has been checked that *a priori* unsafe flags based, for instance, on channels that are known to contain a fraction of a GW signal have a probability well below 10^{-5}. On the other hand, all flags, *a priori* safe but with a probability between 10^{-5} and 10^{-3} were found to be safe, the low probability being due to the effect explained above.

4.3.2. Data quality flag performance. A data quality flag is said to have good performance if it is able to veto glitches affecting an analysis pipeline without vetoing long periods without noise transients. DQ flag performance is measured by considering a set of N_t triggers spanning a large frequency band and the science period T_{tot} of the GW transient searches (the mean trigger rate is $R = N_t/T_{tot}$). Each DQ flag is characterized by the number N_{seg} of disjoint time segments and the total time T_f rejected by the flag. Three figures of merit, discussed in details in [67], are used to measure the flag performance:

(i) **The efficiency** (ϵ) measures the percentage of triggers vetoed by a DQ flag and is given by N_f/N_t, where N_f counts the number of flagged triggers.

(ii) **The use-percentage** (UP) gives the fraction of DQ segments which are actually used to veto triggers and is given by N_{use}/N_{seg}, where N_{use} is the number of segments used to reject at least one trigger. When this number is close to 1,

Category	Definition	Prescription for analyses
CAT1	Flags obvious and severe malfunctions of the detector.	Science data are re-defined when removing CAT1 segments.
CAT2	Flags noisy periods where the coupling between the noise source and the DF is well-established.	Triggers can be automatically removed if flagged by a CAT2 veto. Good performance.
CAT3	Flags noisy periods where the coupling between the noise source and the DF is not well-established.	CAT3 flags should not be applied automatically. Triggers flagged by a CAT3 veto should be followed up carefully.

Table 2. Category definition and prescription for transient GW searches (see section 4.3.2 for more details).

the flagged time period certainly contains a glitch that the DQ flag was designed to veto.

(iii) **The dead-time** $(D = T_f/T_{tot})$ is the percentage of science time rejected by a flag.

It is often convenient to compare the efficiency to the dead-time in order to make sure the flagging is not random. In case of random flagging, $N_f = R \times T_f$ and $\epsilon/D = 1$. On the contrary, if the DQ flag is highly selective for glitches, $\epsilon/D > 1$. Finally, a DQ flag has $\epsilon/D < 1$ if it tends to systematically flag periods of time where no triggers can be found. These figures of merit must be used with care and have limitations. In particular, they are average numbers and they may be biased by large variations of trigger rate or by the segment structure of the DQ flag.

A DQ flag's performance and the level of understanding of its corresponding noise source determine at which stage of a GW search the DQ flag should be applied. DQ flags are divided into three categories: CAT1-3, defined in table 2. When a severe malfunction prevents the detector from working in normal operating conditions, the corresponding period must be discarded from the GW searches. Such CAT1 DQ flags are used to re-define the science segments on which analysis pipelines are run. CAT2 DQ flags are characterized by high performance resulting from a good description of the noise source and its coupling with the DF. CAT2 flags can be applied with confidence to the output of transient GW searches. CAT3 are effective at removing transient noise from the data, but in the presence of a weak physical coupling, caution is exercised when using these flags. Furthermore, CAT3 vetoes typically have an overall larger dead-time than CAT2 flags ($\sim 10\%$). For these reasons, transient GW searches are usually performed in two steps: in the case of CBC searches the search output, with both CAT2 and CAT3 flags applied, is first considered to make statements about the significance of GW candidates or, in the absence of a detection, to derive upper limits on the GW event rate. If no GW candidate is observed, GW candidates after CAT2 flags have been applied are considered. This search is less sensitive, since the noise background is higher, but it allows to ensure that a significant GW event has not been vetoed accidently because of a large dead-time veto. For the burst searches, all triggers after CAT2 flags are taken into account. CAT3 flags are then used when computing their significance [15]. Some addi-

tional DQ flags are uncategorized, because of very low performances or highly uncertain coupling mechanisms. These flags are only considered during the follow-up procedure if a GW event is found to be significant [68]. Further studies of auxiliary channels at the time of the event may rule out an astrophysical origin for the event.

The definition of flags for transient glitches is an iterative process. Most DQ flags are produced online, but from one run to another, the noise coupling can change as new noise sources appear and existing noise is mitigated. The next step is to estimate the performance of the DQ flags used by each data analysis search in order to veto transient features and to determine what noise sources remain after the application of DQ flags. This will be discussed in section 6.1

5. Noise spectral lines

5.1. Investigations

To describe a spectral line, it is common to use the frequency (f_0) and amplitude (A) of the peak maximum. In addition, the line width (W) is the peak width at half maximum, the persistence (P) is the fraction of time the line is visible and the critical ratio (CR) is the difference between the peak amplitude and the mean value of the spectrum, divided by the spectrum standard deviation. Another commonly used parameter is the line energy, which can be defined as the integrated power spectrum of the line over its width, averaged over a given time interval (see [22] for more details). As stated in section 1, we will focus on lines which, unlike those associated to the interferometer internal modes or intentionally added for calibration and control purposes, do not have a well-known origin. Non-stationary lines, with f_0 and/or A varying with time, are particularly troublesome since they are likely to produce transient events or cross the frequency bands of interest for CW searches.

The line hunting and mitigation process follows the detector characterization procedure described in section 3. In addition to generic line tools [23, 24, 25], a dedicated algorithm, NoEMi (Noise Event Miner) [22], has been developed to analyze Virgo data in quasi-real time. NoEMi is based on the algorithms implemented for the CW search. On a daily basis, it analyzes the $h(t)$ channel and a subset of auxiliary channels. NoEMi identifies the noise lines in auxiliary channels and looks for time and frequency coincidences between the DF and these auxiliary channels. A line tracker algorithm reconstructs lines over time, facilitating the follow-up of non-stationary lines. NoEMi displays the latest results (time-frequency plots of the peak maps, lists of lines, and coincidences) on web pages and all the lines are stored in a database [54] which can be accessed offline for further analysis. A web interface is being developed to provide an easy user access to the database. In addition, NoEMi raises an alarm if noise lines are detected at or near the frequency band of the known pulsars of the CW searches. A detailed description of the NoEMi software can be found in [22] and figure 4 shows
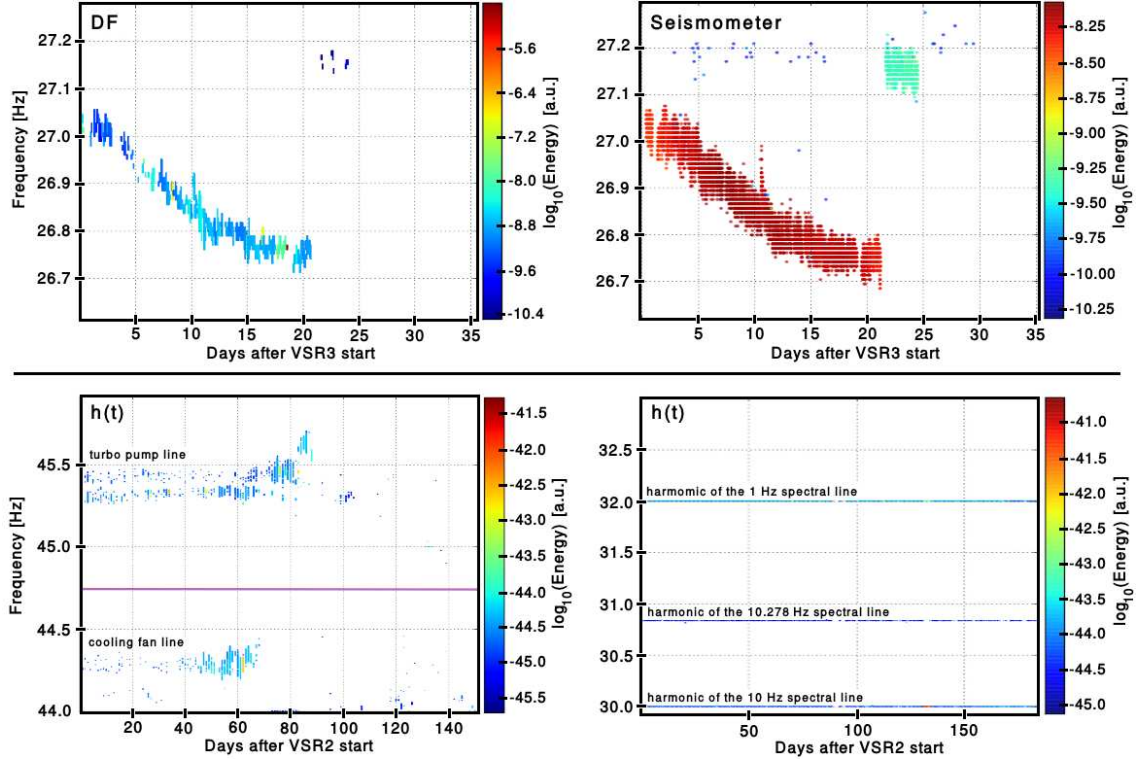
Figure 4. Examples of noise lines reconstructed with NoEMi. The color scale refers to the line energy defined as the integrated amplitude of the line. The upper row shows the coincidence between a noise line seen in the DF channel and in a seismometer during VSR3. The correlation between the two lines allowed for the identification of the noise source as an air-conditioning fan. The lower-left time-frequency plot shows a noise line at ∼44.3 Hz, which was associated with electronic board cooling fans that induce noise currents in the arm mirrors' correction signals. The lines around 45.5 Hz were due to the turbo pump cooling fans vibrations propagating to the DF through scattered light on the vacuum tank walls. These VSR2 lines disappeared after the noise source had been mitigated. The lower-right plot presents stationary harmonics of digital noise spectral lines (1, 10 and 10.278 Hz).

examples of lines detected and followed by NoEMi.

A noise spectral line often results from a mechanical or electronic device operating in a periodic or continuous working cycle. The resulting noise can be of seismic, acoustic and/or magnetic nature. At Virgo, such sources are usually part of the service infrastructure needed for the interferometer operation. This includes machines for air cleaning and conditioning of the experimental areas, vacuum pumps, cooling fluid pumps, small cooling fans for electronic devices, digital clocks regulating data exchange between electronic devices, and the mains power supply. Because of non-linearities in the line generation mechanism or in its coupling to the detector, harmonics (i.e. integer multiples of a line's frequency), as well as linear combinations of the frequency of various lines may appear in the spectrum.

In order to identify the cause of a given line seen in the DF signal it is important to inventory all frequencies occurring on the Virgo site. The typical frequency of AC

electrical motors is a sub-multiple of the power line frequency (50 Hz in Europe), from 12.5 Hz (8-pole engine) to 50 Hz (2-pole). Most engines at the Virgo site are asynchronous which means that their actual rotation frequency is slightly less than described above (i.e. about 45 Hz for cooling fans or about 24 Hz for water pumps). Other mechanical frequencies are also present. For example, the Virgo air-conditioning machines are 4-pole engines that drive large fans via belt and pulley systems, the fan speed is set by the pulleys diameter ratio, typically in the range of 6 Hz to 18 Hz. Higher frequency sources can also be found on the Virgo site. For example, the Virgo ultra-high vacuum system [4] makes use of turbo molecular pumps which rely on a magnetic levitation system to reduce friction; these run between 600 and 1000 Hz. All these frequencies change slightly with time; a few percent variations are observed, resulting from the mains power frequency fluctuations or changing temperature. Harmonics are also generated, as a consequence of non-exact sinusoidal motion due to unavoidable mechanical unbalances.

In the next section we will review the main sources and coupling mechanisms for spectral lines. Since many aspects overlap with the transient noise, we refer to section 4.2 for complementary details.

5.2. Spectral line sources and coupling

5.2.1. Vibration noise. All the machinery operating frequencies constitute a seismic background due to the engine vibrations. The on-site seismic sensors reveal a "forest" of spectral lines up to 600 Hz, whose amplitude roughly decreases as f^{-2}, meaning they have a roughly constant energy content. As explained in section 4.2.1, seismic disturbances are likely to couple to the DF through a variety of mechanisms. It is often not possible to disentangle all of the spectral lines and to link them to a specific noise source. However some couplings were identified and are explained below.

One well-known vibration noise path is located in the injection bench where the laser beam travels a few meters through optical components for shaping and alignment purposes before entering the interferometer. Vibrating optics add angular jitter noise to the beam. Moreover the Virgo in-air input bench has large quality factor (20-40) resonant modes around 15-20 Hz and 45 Hz which are associated with the small rigidity of the supporting legs. These frequencies happen to exactly match the vibration noises of cooling fans (around 45 Hz) and of some vacuum motor fans (18 Hz); the noise is therefore amplified. Mitigation was attempted before VSR2 by moving fan-cooled electronic racks to a separate acoustically-isolated room. Existing optical mounts were also replaced with more rigid ones. By doing this, the resonant modes were shifted to higher frequencies where the vibration noise is weaker. Between VSR1 and VSR2, the accuracy of the interferometer global alignment [60] was improved which also significantly helped reduce alignment noise due to vibrations.

Scattered light often results from vibrating objects such as lenses, vacuum link windows or vacuum pipe walls. As discussed in section 4.2.1, scattered light can be an

important source of noise. If the vibration is periodic, a spectral line will be visible in the DF signal. As an illustration, the lower-left plot of figure 4 shows an example of a noise line caused by scattered light. The line at 45.5 Hz is associated with the vibrations of turbo pump cooling fans which propagate to the vacuum tank walls. This noise was mitigated 90 days after the start of VSR2 by seismically isolating the fans from the vacuum tank.

During VSR1, another source of scattered light was discovered in the detection system; a glass window used to isolate the detection vacuum compartment from the rest of the interferometer was acting as an efficient transducer of seismic and acoustic noise from the external environment to the detector. To cure this problem before VSR2 the window was removed and replaced with a larger aperture pipe with an associated cryogenic pump. Similarly, during VSR2, some light was scattered back into the interferometer by the main beam output window. Improving the quality of the window anti-reflection coating reduced the noise to a negligible level.

Sometimes the noise path of a spectral line cannot be identified. In this case NoEMi can provide useful hints e.g. by connecting a noise line to a noise source based on coincidences with auxiliary channels. For example, during VSR3, the correlation between the frequency variations of a line in the DF and a line detected in a seismometer allowed for the identification of the coupling with the vibration of an air-conditioning fan (see upper row of figure 4). This specific spectral line has been moved out of the detector's sensitive band by reducing the fan rotation speed.

5.2.2. Magnetic noise. Electromagnetic (EM) fields produced by electrical systems are likely to contribute to the noise spectral lines, especially through their magnetic component. The noise strength will depend on the intensity of the field, its frequency and the source distance. Virgo is mostly sensitive to low frequency EM fields (frequencies less than a few hundreds of Hz) which couple directly into the detector bandwidth. At higher frequencies, radio-frequency EM fields are the main source of noise, since a 6.26 MHz frequency is used to phase-modulate the Virgo laser beam. Hence, it is important to keep the frequency region within $\pm$ 10 kHz around the modulation frequency as free as possible of EM noise.

The main magnetic noise entry path is located at the level of the actuators used to control the mirror positions. These actuators are made of coils and magnets which can be disturbed by the presence of a magnetic field and its gradient. During VSR1 small magnetic sources (e.g. power supplies and cooling fans used for the mirrors local control electronics) were located a few meters from the mirrors. The magnetic field radiated by these small magnetic-dipole-like sources decays quickly with distance (as d^{-3}), and so it was sufficient to move them away by a few meters to reduce their effect to a negligible level. After VSR1, to further reduce the magnetic coupling through the actuators, the magnets were replaced with new and less intense ones. It was also determined that the mirror recoil mass, made of aluminum, had an amplification effect on the magnetic field gradient. For VSR3, new recoil masses, made from a dielectric material, were installed.
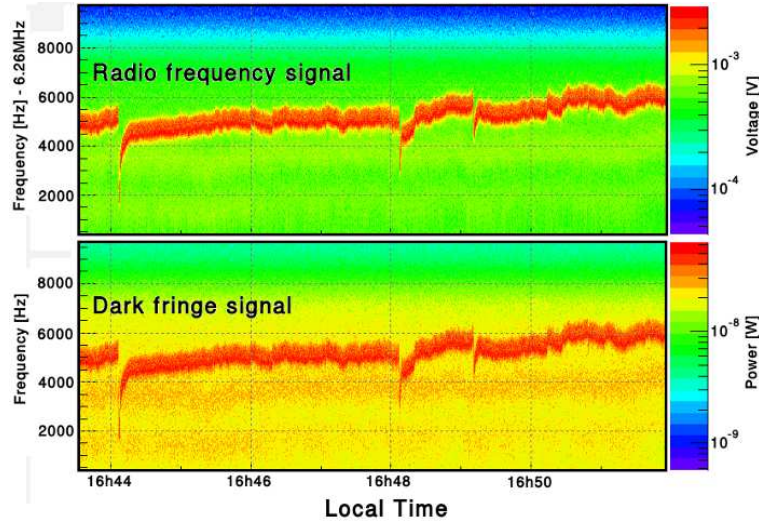
Figure 5. Coupling between a local electromagnetic noise source detected by an antenna (top) and the DF signal (bottom). The noise frequency is very close to the modulation frequency used in Virgo (6.26 MHz) which explains why the noise contaminates the DF signal.

During VSR3, another magnetic noise path was discovered in the fans used to cool down the electronics which compute the mirror position correction. The magnetic field radiated by the fan motors induced a noisy current in the correction signals sent to the actuators which was converted into mirror displacements. This was solved by increasing the distance between the fans and the electronics without compromising the cooling efficiency. The lower-left plot of figure 4 illustrates this problem by showing a frequency line around 44.3 Hz which results from the coupling between the fans and the DF. The line disappeared after 70 days, due to the noise mitigation actions.

As discussed in section 4.2.13, the high-frequency EM fields are likely to couple with the modulated DF signal. During VSR3, an example of a coupling mechanism was identified: environmental sensor ADCs were using a 300 kHz bit-rate serial communication protocol, and the 20$^{\text{th}}$ harmonic of this frequency ($\sim$ 6 MHz) lies a few kHz from Virgo main modulation frequency. A radio-frequency antenna showed a fluctuating line which was seen in time coincidence with the DF signal (see figure 5). An unexpected solution consisted of increasing the temperature of the room hosting the serial link server by 2°. This slightly changed the clock oscillator rate and was sufficient to shift the 20$^{\text{th}}$ harmonic spectral line out of the detector's bandwidth.

5.2.3. Digital noise. Another family of spectral lines is composed of very narrow ($W < 1$ mHz) and stationary lines at multiples of a few fundamental frequencies associated with digital systems in the detector. For instance, several ADC boards used during VSR1 contained a 10 Hz internal clock, which produced a comb of lines spaced by exactly 10 Hz in the frequency domain. These lines were very intense and covered the whole frequency range of interest for CW searches (between 10 Hz and 2 kHz). A
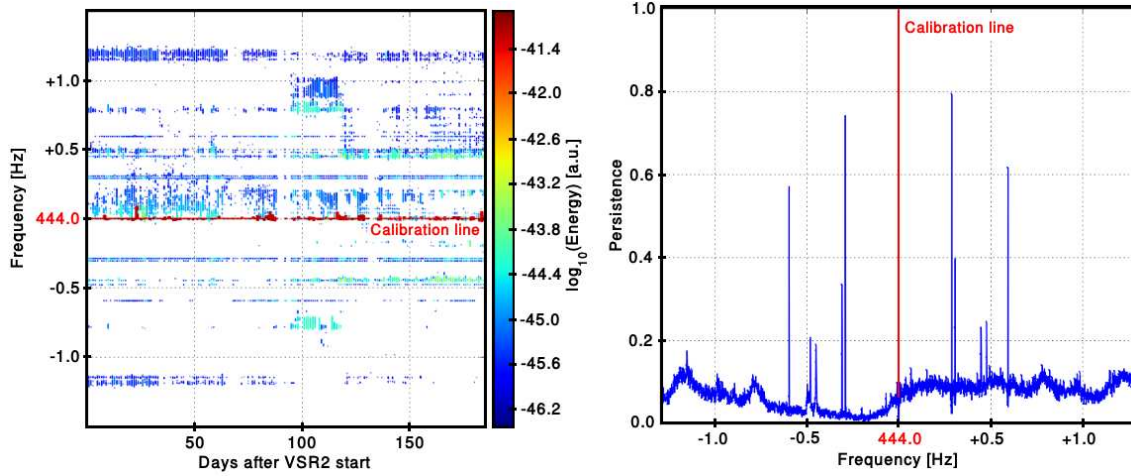
Figure 6. Time-frequency (left) and persistence (right) plots of the sidebands of the 444 Hz calibration line. The persistence plot has been computed over 10 days of VSR2 data, while the time-frequency plot covers the full VSR2 run.

test consisting of switching off the ADCs during data taking confirmed that they were the source of the disturbance, although the noise coupling with the DF was not clearly understood. After the end of VSR1 these ADCs were replaced and almost all the 10 Hz noise lines disappeared in the subsequent runs. Harmonics of 1 Hz were also observed during VSR1. These lines were concentrated at frequencies below 100 Hz and tests indicated that the noise source was probably the same as for the 10 Hz harmonics since this frequency comb also disappeared nearly completely after th ADC replacement. The bottom-right plot of figure 4 shows some remaining harmonics which were still present in VSR2 data despite of the ADC fix.

Another well-known comb of 10.278 Hz harmonics with a digital origin is present in all Virgo runs. The source of the lines has been recently identified in digital modules used to control the mirror coil drivers. There is a strong indication that the coupling mechanism is of electromagnetic nature.

5.2.4. Sideband lines. The strongest lines in the Virgo spectrum are often surrounded by a dense forest of sidebands. This effect was identified as a result of a coupling with the super-attenuator and suspension mechanical modes. For example, figure 6 shows the lines observed on both sides of the 444 Hz injected calibration line and table 3 lists the sideband frequencies associated to each identified mode. The exact mechanism that produces the sidebands is not known, but is likely due to some non-linearity of the interferometer.

δf [Hz]	Mode
±0.200	SA first pendulum mode
±0.285	PR payload θ_Z mode
±0.305	BS payload θ_Z mode
±0.450	SA second longitudinal mode
±0.595	SA pendulum mode (last stage)
±1.200	BS suspension longitudinal mode

Table 3. List of identified sidebands associated to the 444 Hz calibration line for VSR2 run. θ_Z refers to the angular oscillation mode with respect to the beam axis (see also section 2 for acronym definitions).

6. Impact on searches

6.1. Transient GW searches

The LIGO-Virgo data are analyzed by multiple search pipelines. This is motivated by the wide range of GW transient signals expected to be detected by ground-based interferometers. The use of DQ flags and their ability to suppress glitches depends on the GW search features, such as the frequency bandwidth, the use of matched filtering, or multi-detector coherence tests. In principle, the ability of DQ flags to remove glitches in the data should be evaluated for each analysis, and a specific categorization (see section 4.3.2) should be used. However, to simplify DQ categorization work, the Virgo detector performance is studied against only two pipelines: Omega and MBTA. Omega is known to be a good representation of a burst-type pipeline while MBTA is typical of a CBC low-mass search.

Although every search is based on a multi-detector analysis, the performance of a DQ flag is first studied with single detector triggers. The glitches in Virgo data should be excluded, regardless of how LIGO and Virgo data are later combined. As a next step, muti-detector analysis pipelines have ways to estimate the background affecting a coincident or coherent search (see section 6.1.2) and we examine the background triggers coming out of the network analysis pipelines in order to understand the nature of the harmful glitches. A few additional DQ flags resulting from this last step were specifically designed to further reduce the number of loud background triggers.

6.1.1. Data quality flag performance results. Using the category definition and figures of merit described in section 4.3.2, we estimate for each run the performance of the DQ flags used by GW burst and CBC searches, using respectively the triggers delivered by single detector Omega and MBTA online analyses. The list of DQ flags and their category assignment is then prepared for burst [15], CBC low-mass [13] and CBC high-mass searches [69]. The prescription can be different for each analysis. For instance, a DQ flag can be prescribed as CAT2 for burst and high-mass searches while it is used as CAT3 for the low-mass search.

Figure 7 illustrates the DQ flag performance for Omega triggers. These results show significant differences between the Virgo science runs. The first run, VSR1, is characterized by a low number of DQ flags (about 20) but they are able to reject a large fraction of loud events. In fact, most of the rejection is obtained by only one flag and the corresponding noise excess occurred in a single night of VSR1 when the laser power stabilization failed due to a blown fuse. The DQ flag was categorized as CAT2 even though the science time should have been re-defined by removing this noisy period from the start (CAT1). If one takes into account this correction, the sample of triggers to be considered is shown by the dashed white histogram in figure 7. With this consideration, the trigger rejection is limited and mostly effective for high-SNR events. Moreover, the initial trigger rate of VSR1 is very high (2.1 Hz for Omega) and, after applying the DQ flags, remains quite large (10 times larger than in VSR2 for SNR>10).

VSR2 started with a greatly improved knowledge of the detector and of its response to noise. Furthermore the detector glitch rate decreased by a factor of 4 with respect to VSR1; this facilitated the noise investigations. This resulted in a significant increase of the number of DQ flags (more than a hundred), explaining the larger dead-time. This also translates into a larger glitch rejection efficiency: $\epsilon \simeq 70\%$ for SNR>8 while it was only $\epsilon \simeq 10\%$ for VSR1. VSR2 is also characterized by a rejection efficiency which covers a wider range of SNR. Low-SNR events are removed with a non-negligible efficiency which is important for multiple-detector analyses since it is likely that some of the numerous low-SNR events will combine to produce the most significant coincidences.

VSR3 data quality was not as good as VSR2 mostly because of the contrast loss issue explained in section 2. Consequently, the detector had to be set on a new working point which increased scattered-light effects. This created a significant number of glitches seen by Omega at frequencies above 500 Hz for which it was not possible to design a DQ flag, explaining the degraded overall performance of VSR3 DQ flags. As explained in section 4.3.2, if the ratio between the efficiency and the dead-time is larger than one, then DQ flags target glitches with good accuracy. These numbers can be derived from the second row of plots in figure 7. For example, if we consider triggers with SNR>10, CAT2&3 flags give ϵ/D=6.9, 6.8 and 3.4 for VSR1, 2 and 3 respectively.

Glitch families are often characterized by a given frequency which can be measured by Omega. It is therefore possible to sort glitch families and to study the ability of a DQ flag to eliminate them. The frequency plots shown in figure 7 (lower-row) present good flagging efficiencies in specific frequency bins. For example, the piezo glitches of VSR1 detailed in section 4.2.10 are visible at a frequency of ~ 140 Hz and are efficiently rejected. In the VSR2 plot, the efficiency histogram for triggers with SNR>5 exhibits higher efficiency values for frequencies of 210 Hz, 420 Hz, 495 Hz and 840 Hz which correspond to alignment glitches described in section 4.2.6. Finally, the efficiency peaks visible on the VSR3 plot between 500 Hz and 1100 Hz are mainly explained by the good performance of the laser power stabilization flag defined in section 4.2.4.
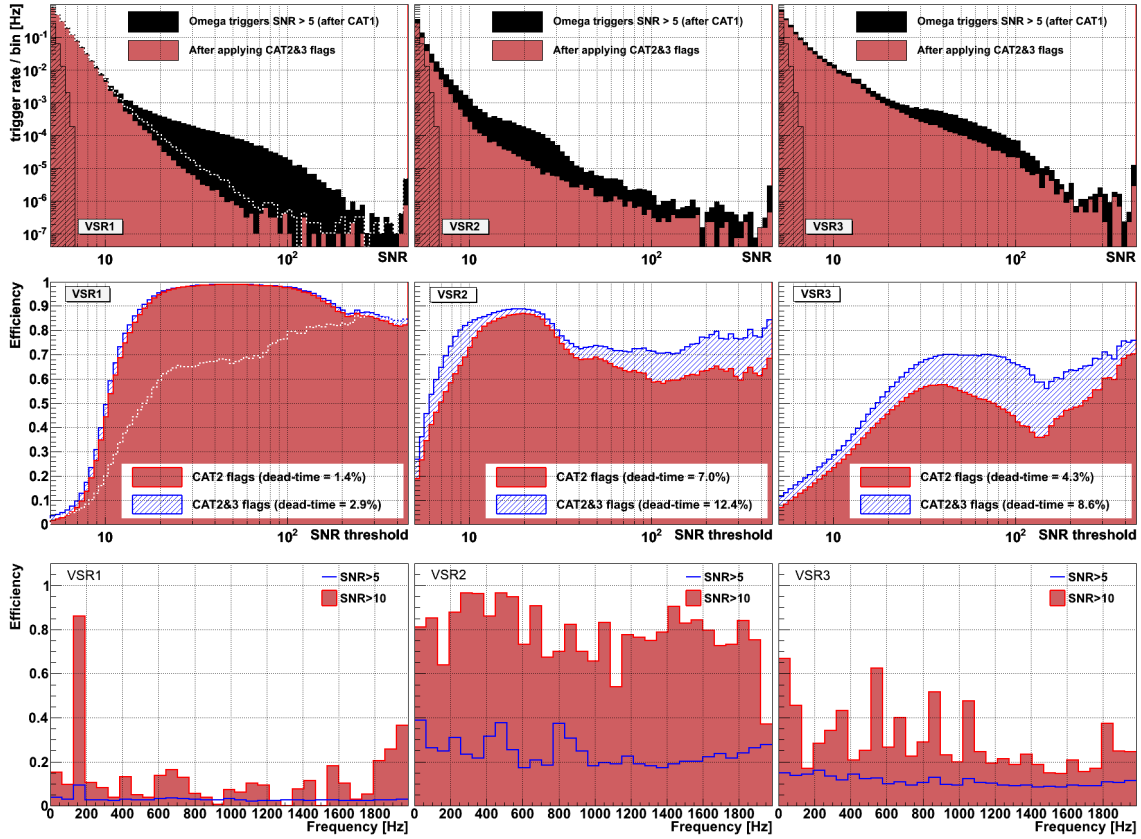
Figure 7. Effect of Virgo DQ flags on Omega triggers for each Virgo run and after CAT1 flags. In the upper row, the black histogram shows the trigger rate in SNR bins while the red distribution shows the trigger rate after CAT2&3 flags. If the VSR1 power stabilization flag had been considered as a CAT1 flag, the initial trigger distribution would have been given by the dashed white histogram. The Omega trigger rate obtained with simulated Gaussian noise is represented by the hashed histogram. The middle row presents the DQ flag rejection efficiency when considering Omega triggers with a SNR above a given threshold. For VSR1, the dashed white histogram shows the CAT2&3 efficiency in the situation where the power stabilization flag is considered as a CAT1 flag. The lower row presents the DQ flag rejection efficiency in bins of the central frequency, as determined by Omega.

6.1.2. Multi-detector analyses. For each trigger, the search pipeline computes a signal-to-noise ratio statistic after applying a coincidence (CBC) or coherence (burst) test to determine if the trigger is present in more than one detector. To measure the background rate of events in the search due to noise, data from the detectors in the network is time-shifted (by an amount greater than the gravitational-wave travel time difference between observatories) and then re-analyzed. Many different shifts are performed to obtain an accurate measure of the background rate in the search. The significance of a candidate GW trigger is characterized by its false alarm rate (FAR), which is computed by comparing the SNR of the candidate trigger to the background. An excess of noise events in a detector can cause the distribution of the background to have a significant non-Gaussian tail at high SNR, thus reducing the significance of GW events. It is

therefore very important to remove loud background events by mitigating them in the detector, or excluding them in the analysis with vetoes. Reducing this non-Gaussian tail in the background is the primary goal of detector characterization, as it increases the astrophysical sensitivity of the search.

Using several detectors in coincidence presents many advantages. The most important one is to reduce the number of background triggers and hence decrease the FAR of GW signals. Initially, it was believed that the coincidence between detectors would be sufficient to reduce the detector noise to its Gaussian component. In fact, it has been realized that searches are limited by accidental coincidences of transient glitches. Thus, noise investigations and DQ flags are very important to improve the sensitivity of the searches. Since VSR1, Virgo data has been used in coincidence with the three LIGO detectors offering multiple coincidence schemes, from 2 to 4 detectors. As an alternative to a basic coincidence between detectors, LIGO and Virgo data can also be combined coherently [70], taking into account the individual detector's antenna patterns. This approach provides an optimal detection efficiency since the network is not limited by the least sensitive detector (at least when combining more than two detectors).

For a network analysis, the performance of DQ flags can differ from what has been obtained with single detector triggers, as presented in section 6.1.1. To study the effect of Virgo DQ flags on multi-detector searches, we chose to consider the coincident CBC low-mass analysis [13] and the coherent all-sky burst search [15]. Only a subset of the data used in the published analyses has been considered to quantify the DQ flags impact. Moreover, only background triggers will be presented in the following. Finally, LIGO DQ flags are never applied in the following studies (except CAT1).

The CBC low-mass analysis makes use of a χ^2 discriminatory test [71] to efficiently reject glitches whose waveform does not match the expected CBC signal. After having selected single detector triggers with a SNR larger than 5.5, a preliminary cut is applied in order to reject events strongly disfavored by the χ^2 test. For triggers with SNR below 12, an additional cut is performed based on the behavior of the χ^2 time series near the trigger time [72]. For the remaining triggers, a reweighted SNR [13] is calculated by down-weighting the SNR progressively with the reduced-χ^2 when reduced-$\chi^2 > 1$. Reweighted SNRs obtained for each detector are summed in quadrature to form the ranking statistic used in the CBC search. To evaluate the Virgo contribution to the CBC statistic and the impact of the DQ flags, both Virgo SNR and Virgo reweighted SNR variables can be considered.

The upper plots on figure 8 show, for VSR2 data, how the Virgo DQ flags perform on low-mass CBC triggers which are coincident in two detectors (Virgo and one of the LIGO detectors). The combination of CAT2&3 flags is able to remove background triggers with an efficiency of 22.6%. The efficiency increases rapidly with the SNR measured in Virgo: $\epsilon = 92.9\%$ for SNR>10 which proves the ability of Virgo DQ flags to remove the loudest CBC triggers. One can note that the loudest triggers are removed
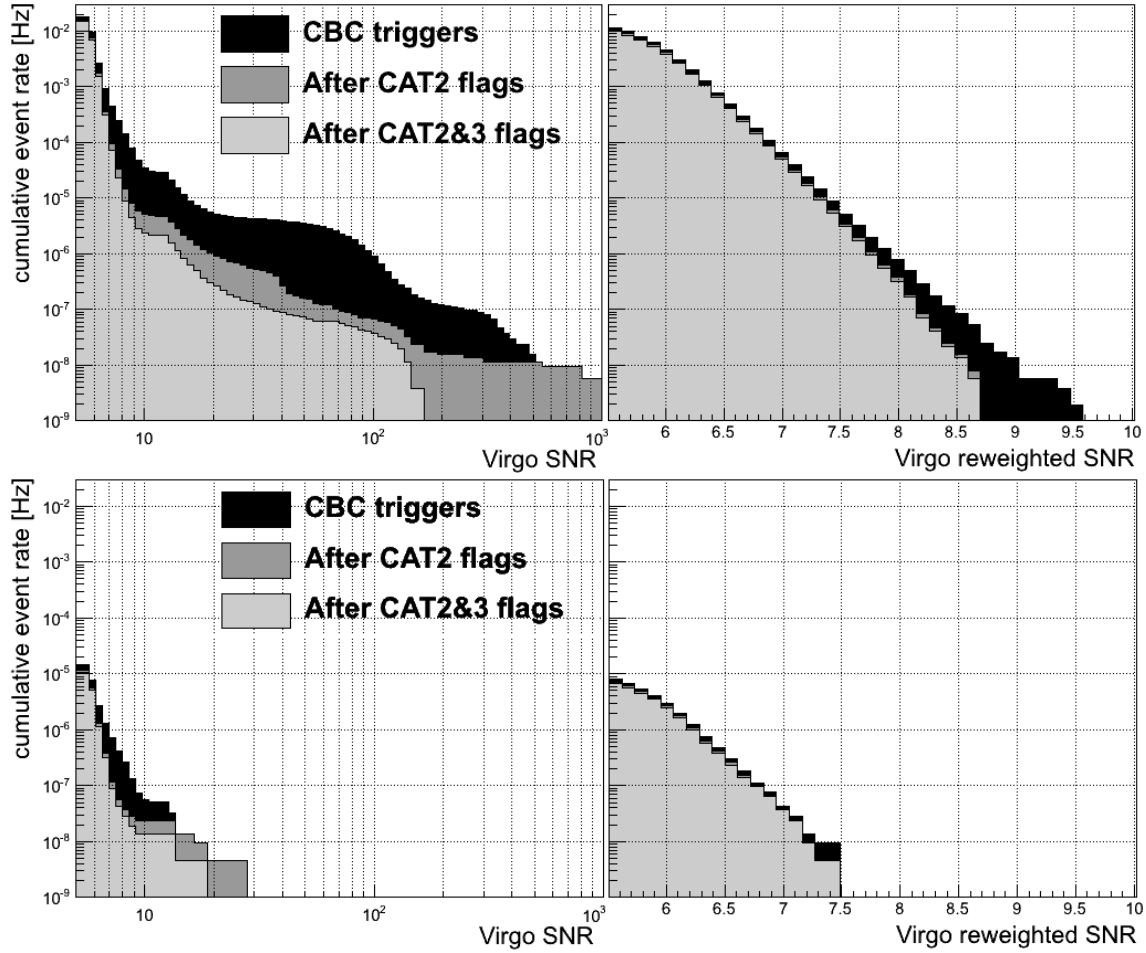
Figure 8. Effect of the Virgo DQ flags on low-mass CBC background triggers. The full VSR2 data sample was considered. Double-coincident (top row) and triple-coincident (bottom row) LIGO-Virgo triggers were used. The left column shows the trigger rate as a function of the Virgo SNR threshold before and after applying CAT2 and CAT3 Virgo DQ flags. On the right column, the events are plotted as a function of the Virgo reweighted SNR which consists of reweighting the Virgo SNR with the reduced-χ^2 [71] of the event (only events with a Virgo reweighted SNR larger than 5.5 are plotted).

by CAT3 flags. These events are found to result from a strong laser disturbance for which a DQ flag was designed. The performance of this flag is too limited to be categorized as CAT2. Many events flagged by a Virgo DQ flag are already disfavored by a high χ^2 value and thus ranked with a low value of reweighted SNR. Nevertheless, the upper-right plot of figure 8 shows that Virgo DQ flags have a non-negligible impact on noise events with large reweighted SNR. For example, when considering CBC triggers with a reweighted SNR above 8, approximately 60% of triggers are removed by Virgo DQ flags. In general, the SNR of the loudest background event allows us to measure the sensitivity of a detector, since a GW candidate must be louder than this to be considered significant. The use of Virgo DQ flags reduced the reweighted SNR of the loudest event from 9.5 to 8.7, leading to an astrophysical volume that is 1.3 times larger than the

search without DQ flags. Although here we only consider the sensitivity of the Virgo detector, and the astrophysical sensitivity depends on all the detectors in the network, this increase in reach is a clear indication of the power of data quality and vetoes.

The initial distribution of CBC triggers visible on the upper-left plot of figure 8 presents some structures which are understood. First, the SNR distribution shows a steep break at SNR=12. This effect results from the analysis feature which consists of applying the χ^2 cuts with a discontinuity at SNR=12. Three populations of glitches then dominate the SNR distribution. The loudest events (SNR>150) correspond to laser disturbances described in section 4.2.4. The large bump with SNR>40 results from an excess of TCS glitches (see section 4.2.7) which are removed by specific DQ flags. Events below SNR=12 (which can also be seen as a bump with Omega triggers in the VSR2 plot of figure 7) are mostly produced by scattered-light mechanisms described in section 4.2.1 and 4.2.6. The DQ flags based on the ground motion velocity and alignment signals are able to remove this population. Moreover, this population of glitches is also characterized by $\chi^2 \sim 1$ (i.e. large reweighted SNR), so these DQ flags are probably the most important flags to improve the sensitivity of the CBC search.

The same study has been performed on triple-coincident events (Virgo and two of the LIGO detectors), as can be seen on the lower row of figure 8. The overall performance remains about the same on triple-coincident CBC events: 30.8% of efficiency. Requiring a triple coincidence offers an even more stringent way to suppress the background than double coincidence, but the reduction concerns all categories of glitches and thus it does not affect the DQ flags rejection efficiency. The lower-right plot of figure 8 shows that the loudest triple background event of the CBC search is not removed by a Virgo DQ flag.

The generic GW burst searches are designed to look for a large variety of transient signals, spanning the full frequency bandwidth of the detectors and without a precise model of waveforms. They are therefore sensitive to a larger number of glitch types than CBC searches and cannot make use of consistency tests such as the χ^2 test. The all-sky search [14, 15] has been performed by several analysis algorithms. Here we use the latest results obtained with the Coherent Wave-Burst (cWB) pipeline [73] which combines coherently the detectors' strain amplitudes. In the cWB search, the network parameters can be derived from a likelihood method based on a network SNR estimator [74] and can be used to characterize and reject noise transients. Finally, events are ranked as a function of the correlated amplitude ρ, which measures the degree of correlation between the detectors for an event. Virgo DQ flags have a significant impact on cWB triggers and greatly improve the search sensitivity. To study this impact, the cWB pipeline was run over two months of VSR2 data (2009, November and December). The winter season of VSR2 was chosen because these data were the most affected by noise.

In the upper row of figure 9, cWB events obtained with a two detector network (Virgo and one of the LIGO detector) are shown. The left plot shows the impact of
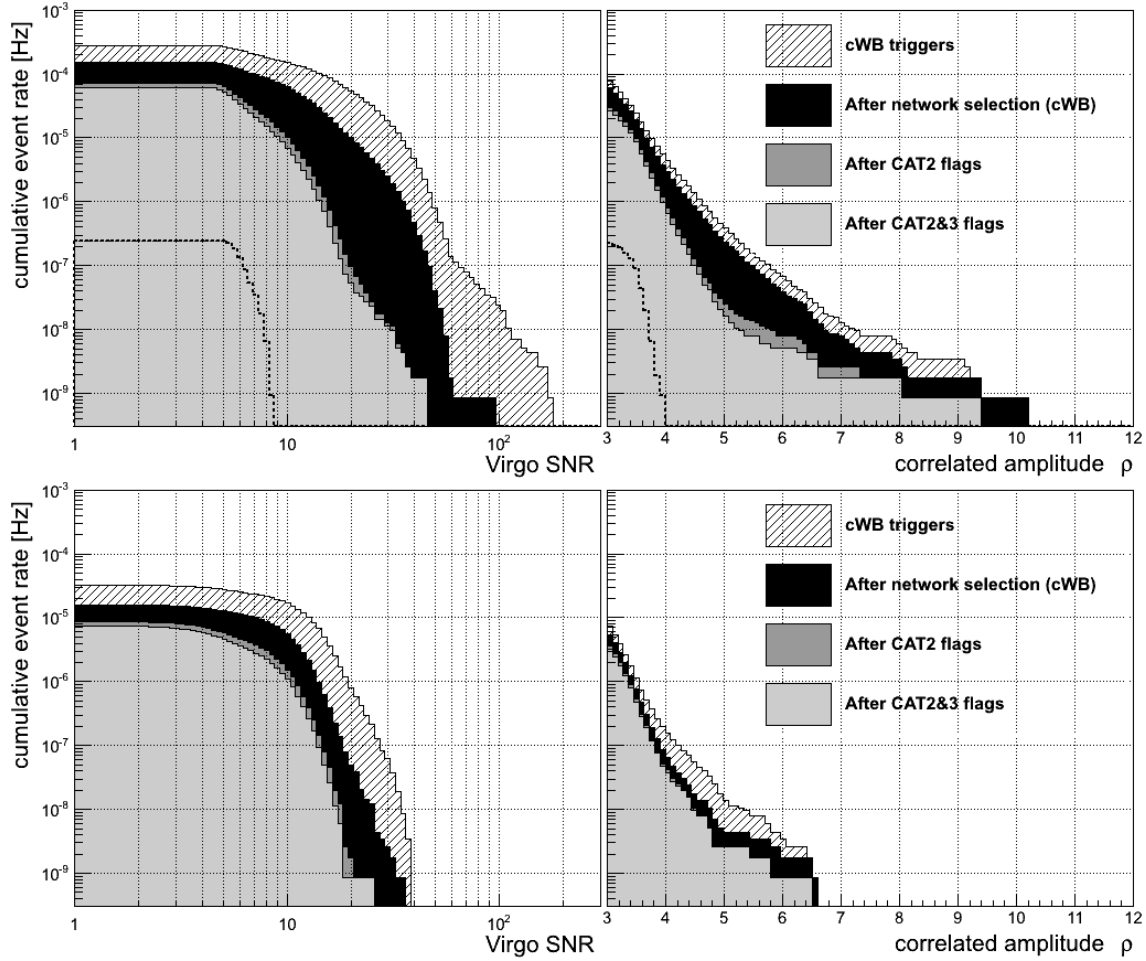
Figure 9. Effect of the Virgo DQ flags on burst-type (cWB) background triggers. Two months of VSR2 background data were considered and coherent LIGO-Virgo event distributions in double coincident time (upper row) and triple coincident time (lower row) are plotted. On the left, the distribution of Virgo SNR, which measures the Virgo contribution to the coherent data stream, is plotted and, on the right, events (with $\rho > 3$) are ranked with the correlated amplitude ρ. The hashed histograms show the trigger rate produced by cWB. When applying cWB selection cuts, it is possible to remove loud triggers, as shown by the black histograms. On top of this selection, applying CAT2 and CAT3 Virgo DQ flags allows for the reduction of the distribution tails even more. The distributions obtained with Gaussian noise are superimposed on double coincident time plots.

DQ flags on the distribution of Virgo SNR which measures the Virgo contribution in the coherent data stream. Firstly, a collection of selection cuts based on the likelihood parameters are implemented in the cWB algorithm which excludes detector glitches incompatible with signals expected from the detector network. This allows for the suppression of the loudest (and most obvious) Virgo glitches. Even with this analysis feature, Virgo DQ flags still efficiently reject part of the remaining triggers. The overall veto efficiency of CAT2&3 flags is 60.4%. For SNR>10, 89.5% of cWB triggers are rejected by Virgo data quality flags. The DQ flag rejection efficiency can be derived

from figure 9 for any Virgo SNR or ρ threshold when neglecting the DQ flags dead-time ($\sim 10\%$). Unlike the CBC analysis, where only a few DQ flags were performing the majority of the rejection, all Virgo DQ flags contribute to the background suppression in the cWB search.

As can be seen in the upper-right plot of figure 9, the Virgo DQ flags are less efficient to remove events ranked with a high ρ mostly because, for these events, the LIGO data strains preponderantly contribute to the coherent stream. Nonetheless, the number of high-ρ events is reduced by Virgo DQ flags. For example, if one fixes the FAR to 1 event per 6 years (rate $\simeq 5 \times 10^{-9}$ Hz), the cWB network selection cuts allow to lower the ρ threshold by 10% and Virgo DQ flags offer an additional 20% of reduction. This represents a gain of sensitive volume of about a factor 2. Such an improvement should be compared with the ideal case corresponding to Gaussian detector noise (also shown on figure 9). Data quality work is increasingly challenging upon approaching this limit. Understanding the glitch production and coupling mechanisms is much more difficult at lower SNRs.

The same study has been performed on cWB triggers produced with a three detectors coherent data stream and results are presented in the lower row of figure 9. As expected, in this configuration, the search is more sensitive since, for a comparable FAR, the ρ threshold can be reduced with respect to the two detector case. For example, with a FAR of 1 event per 6 years, adding a third detector in the network allows for a 30% reduction of the ρ threshold (i.e. the sensitive volume gets twice larger). This threshold can be further lowered by about 10% by the use of Virgo DQ flags (i.e. the sensitive volume gets 30% larger).

6.1.3. Online analyses. During VSR3, the online data quality monitoring took on a new and important dimension. Transient GW searches using LIGO-Virgo data were performed online and alerts were sent to telescopes in order to observe a possible electromagnetic (EM) counterpart which would increase the detection confidence of a GW event [75]. Therefore, the data quality information had to be provided with a very low latency in order to exclude obviously false GW candidates (noise glitches) which would have otherwise been sent to telescopes.

For VSR2 an online architecture, based on tools used for the data acquisition system, was set up to provide DQ flags with a latency of about 30 seconds. These flags were stored in the LIGO and Virgo databases. In parallel, the DQ flags were monitored which allowed scientists in the control room during VSR3 to rapidly check data quality to make the decision whether or not to send an alert for prompt EM follow-up.

The main requirements for online DQ flags are: the reliability of the online production system, the possibility of using the processing algorithm both online and offline, and the ability to provide a complete data quality information while at low latencies. During VSR2 and VSR3, the online DQ production did not encounter major problems and had a duty cycle similar to the Virgo data acquisition system (above 99.8%). The algorithms producing the DQ flags used generic I/O libraries and thus

have also reprocessed missing segments. Finally, the most difficult part of the DQ flag production concerns the confidence of the data quality information provided with low latency. A software architecture has been created to provide online DQ monitoring. This allowed for the selection of the most reliable flags in order to veto events before sending alerts to telescopes. To improve this architecture and to provide accurate online DQ flags will be one of the main challenges for Advanced Virgo [47].

One strong constraint on the online DQ flags is the daily variation of the glitch rate and glitch types, depending on e.g. the detector working point or the weather conditions. Online DQ flags performance can vary significantly if they are not tuned on the fly. Automatization of such tuning will be an important step to provide the required reliability of DQ flags for the Advanced Virgo online analyses.

6.1.4. Remaining glitches. The study of data quality is a challenging task and many families of glitches have origins which have not been identified. For instance, many Omega scans performed on the VSR2 data show a recurrent glitch around 60 Hz that always has the same morphology in the time-frequency plane. It is very likely that these glitches have a common source of noise. However, no explanation for these glitches has been found.

The lack of understanding of a noise source and of the coupling to the DF is, in most cases, due to the fact that no auxiliary channel is correlated with the DF glitches. There are three possible scenarios which can result in unknown glitch families:

 (i) The detector or the environment is not fully monitored: the noise source and the coupling mechanism cannot be detected by any of the current sensors. This explains why no auxiliary channel has been found to be sensitive to this noise.

 (ii) The sensitive channel is actually operational, but it is also sensitive to many other kinds of noise which do not affect the GW data. In that case, the effective signal component is swamped by uninteresting noise and it is highly unlikely that this channel will be identified as useful for glitch flagging.

(iii) The current flagging procedure mostly relies on a glitch-to-glitch method. Only a few examples of DQ flags are defined by more advanced approaches (for example the scattered-light glitches) resulting from a complete understanding of the noise path. In the future, it may be necessary to explore more non-linear coupling hypotheses (see section 7 for further discussions).

As can be seen on figure 10, most of the remaining glitches do not seem to be associated with a given permanent noise source that could have been associated with a specific frequency band. After applying the DQ flags, the low frequency region remains the most contaminated: triggers with a frequency below 300 Hz represent 89% of the remaining triggers. The "60 Hz glitches" mentioned above represent about 12% of the remaining low frequency glitches. Figure 10 also displays a sudden drop of the trigger rate at mid-run. On October 5th 2009, a short commissioning break occurred during which several actions were performed (dust cover installation, laser and TCS
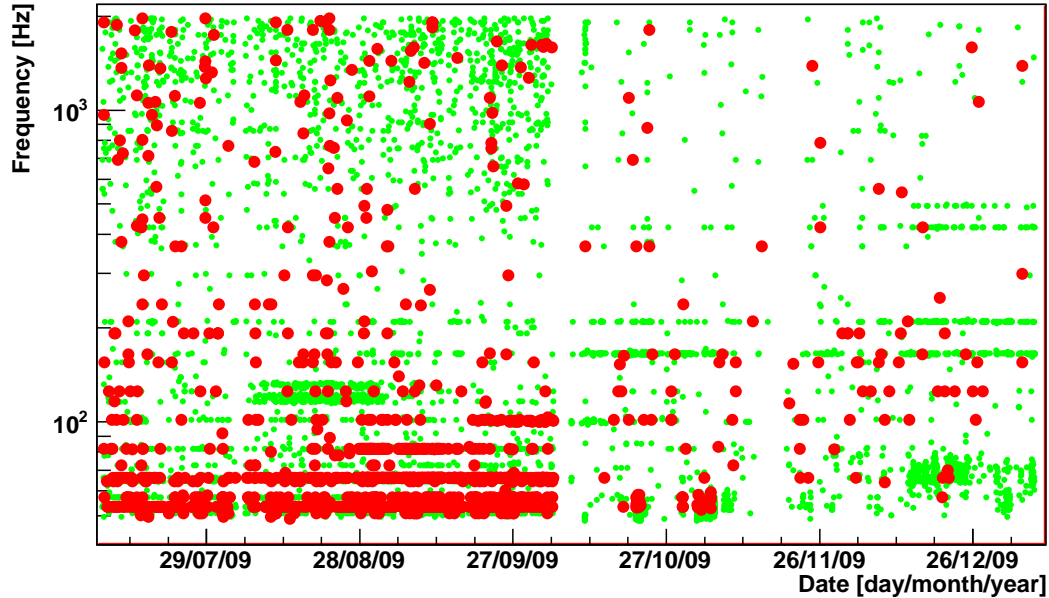
Figure 10. Time-frequency distribution of the remaining VSR2 Omega triggers (from 48 Hz to 2048 Hz) with SNR>10 after having applied the CAT2&3 DQ flags (green dots). Triggers with SNR>20 are represented with a red full circle.

maintenance) and the exact reason for the glitch rate reduction has never been well-established.

6.2. Continuous wave searches

6.2.1. Targeted searches. Given the sensitivity of the first generation of interferometers, only a few known pulsars are astrophysically relevant for close examination [17, 19]. For these pulsars, even in the case of a null detection, it is possible to approach and possibly beat the so-called spin-down limit. To achieve this goal, it is important to make sure that no noise spectral line crosses the frequency band of these targeted pulsars. This task was performed by the NoEMi software described in section 5.1. In table 4, known pulsars monitored in the last Virgo science runs are listed.

During VSR2 a non-stationary noise line affected the sensitivity of the Virgo detector at the frequency of the Vela pulsar (22.38 Hz) as shown on the left plot of figure 11. The disturbance caused a loss of sensitivity of about 20% [19]. Running the NoEMi coincidence analysis on the auxiliary channels led to evidence that the disturbance was correlated with a line (actually a doublet of lines), clearly visible in the data of an accelerometer monitoring the vibrations of the TCS optical benches (see right plot on figure 11). Although a satisfactory description of the noise coupling mechanism was not achieved, the source of the disturbance was identified as being two chillers (pumps that circulate a cooling fluid for the TCS laser) located near the TCS room. The rotation frequency of the chiller engine was indeed 22.4 Hz. The vibration was probably transmitted to the TCS bench through the cooling pipes. During VSR3

| Name	f_0 [Hz]
PSR J0835-4510 (Vela)	22.38
PSR J0205+6449	30.42
PSR J1833+1034	32.31
PSR J1747-2809	38.36
PSR J1813-1749	44.73
PSR J1952+3252	50.59
PSR J1913+1011	55.70
PSR B0531+21 (Crab)	59.47
PSR J1400-6325	64.14

Table 4. Known pulsars monitored by NoEMi. f_0 is the expected frequency of the GW signal, equal to twice the spin frequency. The pulsar frequency bands ($\Delta f \simeq 10^{-4} f_0$) are constantly monitored during data taking and an alarm is raised if they are contaminated by a noise line. This happened during VSR2 and VSR4 runs for Vela, and during VSR4 for PSR J1952+3252.
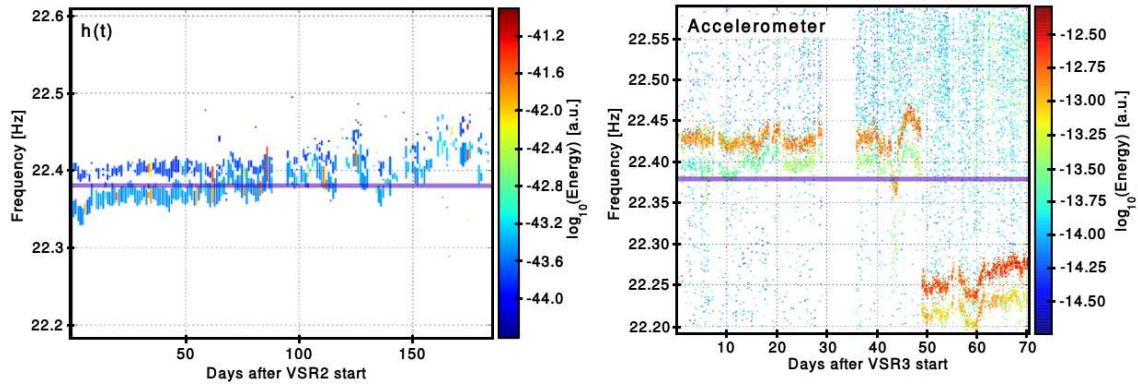
Figure 11. NoEMi plots showing the Vela frequency band crossed by noise spectral lines. The left plot shows the evolution of the noise lines during VSR2. The plot on the right shows the same noise detected by an accelerometer, which helped to identify the source of the vibration disturbance caused by a chiller. The rotation frequency of the chiller engine has been changed to move the noise line out of the Vela frequency band.

the noise line was no longer visible in the DF, although it was still present in the accelerometer. It is assumed therefore that the line was hidden under the detector noise, which at the Vela frequency was 2 to 3 times worse with respect to VSR2. A small but indicative coherence was indeed found between the DF and the accelerometer data. To remove the disturbance away from the Vela band a variable frequency drive was installed during VSR3 to change the rotation frequency of the chiller engines, as can be seen in the right plot of figure 11.

6.2.2. All-sky searches. All-sky searches produce a list of CW "candidates", characterized by a position in the sky, a signal frequency and one or more frequency
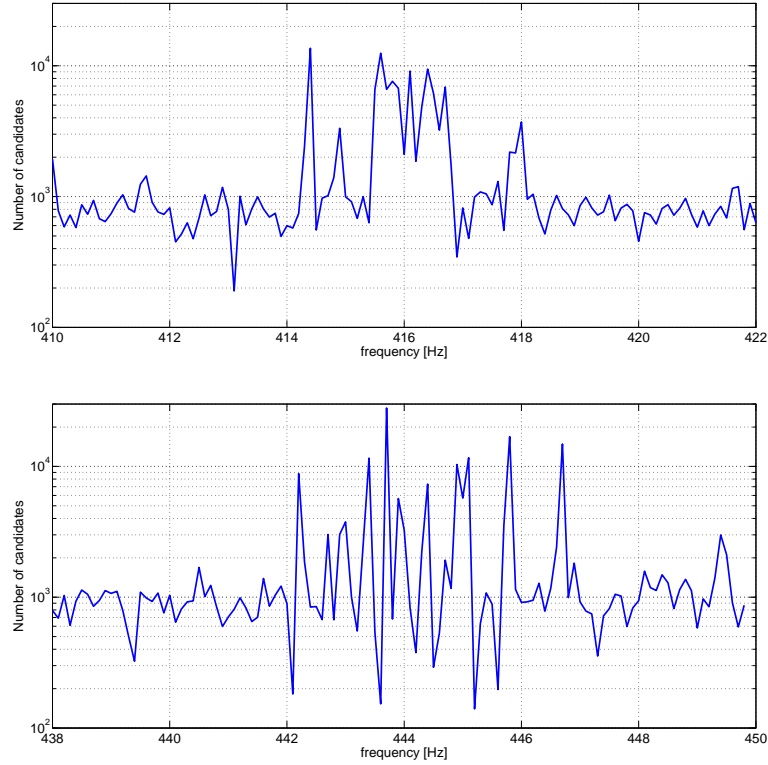
Figure 12. All-sky CW candidates found in the 410-422 Hz (top) and 438-450 Hz (bottom) frequency bands during VSR1 (bin width = 0.1 Hz). The excess of candidates around 416 Hz and 444 Hz have a known instrumental origin.

derivatives (spin-down). A follow-up of those candidates is performed in the next step of the analysis [76, 77, 78]. More precisely, candidate events are selected by thresholding on a quantity characterizing the candidate significance (using Hough maps built in the source parameters space). If a noise line is present in the data, it shows up as a collection of fake candidates. Even a very narrow and constant frequency line produces multiple candidates in a frequency band around it and for various spin-down values. This effect is even larger in the case of broader lines or a forest of narrow lines, like the sidebands described in section 5.2.4. A sufficiently high threshold on the line significance helps to maintain a reasonable number of candidates but reduces the sensitivity of the search. For example, figure 12 shows the number of CW candidates selected during VSR1 in the 410-422 Hz and 438-450 Hz frequency bands. Two excesses of candidates are clearly visible. The first one, around 444 Hz, is associated with a calibration line and its sidebands, discussed in section 5.2.4. The second excess, around 416 Hz, corresponds to the 10$^{\text{th}}$ harmonic of a 41.618 Hz noise line and its sidebands. There are strong indications that this noise line is due to vibrations of the external injection optical bench producing some beam jitter [79].

To reduce the number of signal candidates, it is crucial to produce lists of frequency intervals affected by noise disturbances described in section 5.2. One should add to this

	Line categories	Number of identified lines
Intrinsic lines	Violin modes	127
	Mechanical resonances	26
	Calibration and control	32
Noise lines	Power line and harmonics	40
	Vibration	24
	Magnetic	–
	Digital	73
	Sidebands	640

Table 5. Number of identified lines (over a total of 1390 lines) for each category in VSR3 data.

list all the lines associated with the intrinsic resonances of the interferometer as well as the injected lines used for calibration and control. To achieve this task, all the lines detected by NoEMi are reviewed and identified one by one. This work is still in progress. Table 5 presents the current status of the lines identification in VSR3 data. 962 lines have been identified and about 400 lines still remain to be classified. Once this work is finished, the frequency bin corresponding to each identified line will be discarded before running the all-sky CW analysis.

7. Conclusion and perspectives

For several years, the Virgo detector has been operational either in commissioning mode, for various enhancements and tunings, or in science mode for four scientific runs in coincidence with the LIGO and GEO detectors. During this time, investigations have been performed to improve the overall detector sensitivity and the noise stationarity. Significant efforts have been made to understand and mitigate the sources of noise transients and spectral lines that reduce the sensitivity of GW searches. Virgo noise events present in the data have been efficiently rejected by defining DQ flags or by tracking noise spectral lines. Such work has provided good results and has improved the astrophysical reach of each scientific run.

Since the first scientific run, VSR1, a set of vetoes, mainly based on DQ flags, have been set up using the monitoring and investigations made on glitches detected by the online analyses MBTA and Omega. The DQ flags defined for Virgo data have shown a high rejection efficiency for noise transients and significantly enhanced the sensitivity of CBC and bursts multi-detector searches. For instance, during the VSR2 run, Virgo triggers with SNR>10 were rejected with an efficiency of 92.9% and 89.5% for CBC low-mass and all-sky bursts searches respectively. It has been shown that the level of glitch rejection achieved by this work has allowed a significant reduction in the noise background of the transient searches. Although a full study of the astrophysical sensitivity of the network is outside the scope of this paper, these improvement in data quality can significantly increase the sensitivity of searches for GWs.

CW search sensitivity can be significantly improved by removing noise spectral lines

contaminating the data. A monitoring tool (NoEMi [22]) has been developed in order to spot and track noise spectral lines. Whenever possible, lines whose source were identified during the data taking were mitigated or removed from the detector's data. All lines are stored in a database which can be accessed offline to work on their identification. The frequency bins overlapping with identified lines were eventually vetoed in the CW all-sky analysis.

Over four scientific runs, the characterization of Virgo data quality provided for a deep understanding of the Virgo detector and the properties of its noise. Many noise sources and couplings to the DF have been fully described. It has been realized that data quality is an essential feature of the data analysis process, without which it is impossible to distinguish GW events from the data with sufficient confidence. All the tools developed for glitch and line hunting taught us much, not only about the detector and its various noise coupling paths, but also how the noise hunting, mitigation and flagging should be conducted. We also acknowledged the limitations of our current noise characterization procedures.

The experience gained with the first generation of detectors will be a great asset when applied to the up-coming Advanced Virgo experiment [47], even if noise sources and couplings are expected to significantly differ from those of Virgo. Before resuming science in 2015, many projects are expected to be developed in order to improve the detector characterization methods and to optimize the use of the data quality information in GW searches. Firstly, DQ flags used by transient GW searches could be better optimized. For example, the duration of flagged segments could be adapted to the glitch type they target. Auxiliary channel monitors also need to be finely tuned and, for that purpose, investigation campaigns are foreseen to take place before scientific runs. Finally, the use of DQ flags by search pipelines could be revisited. Efforts will be needed to develop tools able to prescribe a DQ flag category specifically tailored for a given GW search. More ambitiously, all the data quality information could be combined into a single parameter assigning a probability for an event to be an instrumental glitch. This parameter could then be folded in the ranking statistic of every transient GW search. For the line hunting, NoEMi will be further improved. Some tasks, like the identification of lines belonging to the same family (e.g. the sidebands mentioned in section 5.2.4 or the combs of digital lines described in section 5.2.3), will be automatized. For the all-sky CW analysis, it is foreseen that the search will be conducted with a higher frequency resolution. This implies the need to increase the resolution of the noise line analysis, and therefore the capability to manage a larger number of noise lines.

New tools for noise investigations are currently being studied. For example, glitch classifiers and multi-variate analyses represent a promising improvement for detector characterization [80, 81, 82]. As stated in section 6.1.4, non-linear couplings will require to be better studied. They are strongly suspected to be a major glitch production mechanism. Very few tools are available to systematically track such effects. Nevertheless, many other effects remain uncovered: slowly time-drifting signals, signal

derivative, signal cancellations, linear combinations of auxiliary signals, etc. Along the same line of investigation, and as stated in section 4.1, short time scale non-stationary lines or couplings are sources of glitches and a tool will be specifically needed for them.

For advanced detectors, online analyses will play a major role. The improved sensitivity of the detectors will provide access to many more promising targeted sources among the known pulsar population for CW searches (of the order of 100) [83]. Realistic estimations anticipate that $\sim$ 40 binary neutron star coalescence events should be detectable by the advanced LIGO-Virgo detectors network per year [84]. Alerts will be sent to telescopes or satellites for electromagnetic follow-up as soon as significant GW transient candidates are detected. It is therefore mandatory to provide the most efficient and reliable online data quality information as possible. Data quality online architectures have been tested since VSR2 for both noise line and transient events. Pulsar frequency bands have been kept under close surveillance and DQ flags have been produced with a latency of about 30 s. Online monitoring will be further improved with the addition of new tools for glitches and lines identification. It will help to provide fast identification followed by mitigation or veto of noise transients and spectral lines. Several projects are already in progress in order to perform detector characterization as reactively and quickly as possible and to coordinate efficiently the data quality operations.

Many projects and hard work will be needed to improve the detector characterization and to optimize the use of the data quality information for Advanced Virgo. A decisive era for GW physics is about to begin, where reliable and reactive data quality information will represent a key element to grant due confidence to the first GW event detection.

References

[1] Arai K and the TAMA Collaboration 2008 *JPCS* **120** 032010
[2] Abbott B *et al.* 2009 *Rep. Prog. Phys.* **72** 076901
[3] Grote H and the LIGO Scientific Collaboration 2010 *Class. Quantum Grav.* **27** 084003
[4] Accadia T *et al.* (Virgo Collaboration) 2012 *JINST* **7** P03012
[5] Thorne K S 1987 Gravitational radiation *Three Hundred Years of Gravitation* ed Hawking S and Israel W (Cambridge; New York: Cambridge University Press) pp 330–458
[6] Ott C 2009 *Class. Quantum Grav.* **26** 204015
[7] Kokkotas K D and Schmidt B 1999 *Living Rev. Rel.* **2**
[8] Lindblom L, Owen B and Morsink S 1998 *Phys. Rev. Lett.* **80** 4843–4846
[9] Bondarescu R, Teukolsky S and Wasserman I 2007 *Phys. Rev. D* **76** 064019
[10] Glampedakis K, Samuelsson L and Andersson N 2006 *Monthly Notices of the Royal Astronomical Society* **371** L74–L77
[11] Damour T and Vilenkin A 2005 *Phys. Rev. D* **71** 063510
[12] Abadie J *et al.* (LIGO Scientific Collaboration and Virgo Collaboration) 2010 *Phys. Rev. D* **82** 102001
[13] Abadie J *et al.* (LIGO Scientific Collaboration and Virgo Collaboration) 2012 *To be published Phys. Rev. D* (*Preprint* `arXiv:gr-qc/1111.7314`)
[14] Abadie J *et al.* (LIGO Scientific Collaboration and Virgo Collaboration) 2010 *Phys. Rev. D* **81** 102001
[15] Abadie J *et al.* (LIGO Scientific Collaboration and Virgo Collaboration) 2012 *To be published Phys. Rev. D* (*Preprint* `arXiv:gr-qc/1202.2788`)
[16] Prix R 2009 *Neutron Stars and Pulsars* (ed. W. Becker, Springer-Verlag)
[17] Abbott B *et al.* (The LIGO Scientific Collaboration and the Virgo Collaboration) 2010 *Astrophys. J.* **713** 671–685
[18] Abbott B *et al.* (The LIGO Scientific Collaboration) 2008 *Astrophys. J.* **683** L45–L50
[19] Abadie J *et al.* (The LIGO Scientific Collaboration, the Virgo Collaboration) 2011 *Astrophys. J.* **737** 93
[20] Palomba C, the LIGO Scientific Collaboration and the Virgo Collaboration 2011 Searches for continuous gravitational wave signals and stochastic backgrounds in ligo and virgo data *46th Rencontres De Moriond: Gravitational Waves And Experimental Gravity 20-27 Mar 2011, La Thuile, Aosta Valley, Italy* (*Preprint* `arXiv:astro-ph.IM/1201.3176`)
[21] Acernese F *et al.* (Virgo Collaboration) 2009 *Class. Quantum Grav.* **26** 204002
[22] Accadia T *et al.* (Virgo Collaboration) 2012 *JPCS* **363** 012037
[23] Coughlin M, the LIGO Scientific Collaboration and the Virgo Collaboration 2010 *JPCS* **243** 012010
[24] Acernese F *et al.* (Virgo Collaboration) 2005 *Class. Quantum Grav.* **22** S1189
[25] Acernese F *et al.* (Virgo Collaboration) 2005 *Class. Quantum Grav.* **22** S1041
[26] Grishchuk L P 1974 *Sov. Phys. - JETP* **40** 409
[27] Kosowsky A, Turner M and Watkins R 1992 *Phys. Rev. Lett.* **69** 2026–2029 revised version
[28] Caldwell R and Allen B 1992 *Phys. Rev. D* **45** 3447–3468 revised version
[29] Ferrari V, Matarrese S and Schneider R 1999 *Monthly Notices of the Royal Astronomical Society* **303** 247
[30] Regimbau T and de Freitas Pacheco J 2006 *Astron. Astrophys.* **447** 1

[31] Regimbau T and de Freitas Pacheco J 2006 *Astrophys. J.* **642** 455–461

[32] Christensen N 1992 *Phys. Rev. D* **46** 5250–5266

[33] Allen B and Romano J 1999 *Phys. Rev. D* **59** 102001

[34] Abadie J *et al.* (LIGO Scientific Collaboration and Virgo Collaboration) 2012 *Phys. Rev. D* **85**(12) 122001

[35] Accadia T *et al.* (Virgo Collaboration) 2010 *JPCS* **228** 012015

[36] Accadia T *et al.* (Virgo Collaboration) 2011 *Class. Quantum Grav.* **28** 025005

[37] Acernese F *et al.* (Virgo Collaboration) 2010 *Astroparticle Physics* **33** 182 – 189

[38] Bondu F, Brillet A, Cleva F, Heitmann H, Loupias M, Man C, H T and the Virgo Collaboration 2002 *Class. Quantum Grav.* **19** 1829

[39] Acernese F *et al.* (Virgo Collaboration) 2009 *Phys. Rev. A* **79**(5) 053824

[40] Vinet J Y, Brisson V, Braccini S, Ferrante I, Pinard L, Bondu F and Tournié E 1997 *Phys. Rev. D* **56**(10) 6085–6095

[41] Drever R, Hall J, Kowalski F, Hough J, Ford G, Munley A and Ward H 1983 *Appl. Phys. B* **31**(2) 97–105

[42] Acernese F *et al.* (Virgo Collaboration) 2008 *Astroparticle Physics* **30** 29 – 38

[43] Accadia T *et al.* (Virgo Collaboration) 2011 *Astroparticle Physics* **34** 521 – 527

[44] Acernese F *et al.* (Virgo Collaboration) 2007 Noise budget and noise hunting in Virgo *2007 Gravitational Waves and Experimental Gravity* ed Dumarchez, J, Trân Thanh Vân, J pp 147–152

[45] Chatterji S 2005 *The search for gravitational wave bursts in data from the second LIGO science run* Ph.D. thesis Massachusetts Institute of Technology URL `http://hdl.handle.net/1721.1/34388`

[46] Accadia T *et al.* (Virgo Collaboration) 2010 A Thermal Compensation System for the gravitational wave detector Virgo ed Damour, T, Jantzen, RT, Ruffini, R pp 1652 – 1656

[47] URL `https://wwwcascina.virgo.infn.it/advirgo/`

[48] Lorenzini M and the Virgo Collaboration 2010 *Class. Quantum Grav.* **27** 084021

[49] Vajente G 2008 *Analysis of sensitivity and noise sources for the Virgo gravitational wave interferometer* Ph.D. thesis Scuola Normale di Pisa

[50] Leroy N, the LIGO Scientific Collaboration and the Virgo Collaboration 2009 *Class. Quantum Grav.* **26** 204007

[51] Robinet F, the LIGO Scientific Collaboration and the Virgo Collaboration 2010 *Class. Quantum Grav.* **27** 194012

[52] Christensen N, the LIGO Scientific Collaboration and the Virgo Collaboration 2010 *Class. Quantum Grav.* **27** 194010

[53] URL `https://vdb.virgo.infn.it/main.php`

[54] URL `https://pub3.virgo.infn.it/MonitoringWeb/Noise/html/index.php?callContent=408`

[55] Buskulic D, the LIGO Scientific Collaboration and the Virgo Collaboration 2010 *Class. Quantum Grav.* **27** 194013

[56] Accadia T *et al.* (Virgo Collaboration) 2010 *Class. Quantum Grav.* **27** 194011

[57] Coughlin, M and the LIGO Scientific Collaboration and the Virgo Collaboration 2011 *Class. Quantum Grav.* **28** 235008

[58] Ballinger T, the LIGO Scientific Collaboration and the Virgo Collaboration 2009 *Class. Quantum Grav.* **26** 204003

[59] Acernese F *et al.* (Virgo Collaboration) 2010 *Astroparticle Physics* **33** 131 – 139

[60] Accadia T *et al.* (Virgo Collaboration) 2011 *Astroparticle Physics* **34** 327 – 332

[61] Bizouard M A, Cavalier F, Christensen N, Clapson A and Hello P 2007 Data quality and veto studies for the all-sky gravitational wave burst search in Virgo C7 Run data Tech. Rep. VIR-0013D-07

[62] Acernese F *et al.* (Virgo Collaboration) 2008 *Class. Quantum Grav.* **25** 184003

[63] Chatterji S *et al.* 2004 *Class. Quantum Grav.* **21** S1809

[64] Isogai T, the LIGO Scientific Collaboration and the Virgo Collaboratio 2010 *JPCS* **243** 012005
[65] Smith J, Abbott T, Hirose E, Leroy N, MacLeod D, McIver J, Saulson P and Shawhan P 2011 *Class. Quantum Grav.* **28** 235005
[66] URL `https://pub3.ego-gw.it/logbook`
[67] Slutsky J *et al.* 2010 *Class. Quantum Grav.* **27** 165023
[68] Gouaty R and the LIGO Scientific Collaboration 2008 *Class. Quantum Grav.* **25** 184006
[69] Abadie J *et al.* (LIGO Scientific Collaboration and Virgo Collaboration) 2012 *Phys. Rev. D* **85**(10) 102004
[70] Arnaud N, Barsuglia M, Bizouard M A, Brisson V, Cavalier F, Davier M, Hello P, Kreckelbergh S and Porter E 2003 *Phys. Rev. D* **68**(10) 102001
[71] Allen B 2005 *Phys. Rev. D* **71**(6) 062001
[72] Rodriguez A 2008 (*Preprint* `arXiv:gr-qc/0802.1376`)
[73] Klimenko S, Yakushin I, Mercer A and Mitselmakher G 2008 *Class. Quantum Grav.* **25** 114029
[74] Klimenko S, Mohanty S, Rakhmanov M and Mitselmakher G 2005 *Phys. Rev. D* **72**(12) 122002
[75] Abadie J *et al.* (The LIGO Scientific Collaboration, the Virgo Collaboration) 2012 *Astron. Astrophys.* **539** 184006
[76] Astone P, Frasca S and Palomba C 2005 *Class. Quantum Grav.* **22** S1197
[77] Palomba C, Astone P and Frasca S 2005 *Class. Quantum Grav.* **22** S1255
[78] Acernese F *et al.* (Virgo Collaboration) 2007 *Class. Quantum Grav.* **24** S491
[79] Acernese F *et al.* (Virgo Collaboration) 2007 *Class. Quantum Grav.* **24** S433
[80] Mukherjee S and the LIGO Scientific Collaboration 2007 *Class. Quantum Grav.* **24** S701
[81] Stroeer A, Blackburn L and Camp J 2011 *Class. Quantum Grav.* **28** 155001
[82] Costa C A and Torres C V 2011 (*Preprint* `arXiv:physics.data-an/1111.4516`)
[83] Pitkin M 2011 *Monthly Notices of the Royal Astronomical Society* **415** 1849–1863
[84] Abadie J *et al.* 2010 *Class. Quantum Grav.* **27** 173001